AGU100 ADVANCING EARTH AND SPACE SCIENCE

JGR

Journal of Geophysical Research: Earth Surface

RESEARCH ARTICLE
10.1029/2017JF004327

Key Points:
- EER (extremely energetic rockfalls) are characterized by explosive fragmentation. Information on EERs from different sources is provided
- Physical models are suggested for the description of different sequences of EERs, including air blast and rock powder cloud propagation
- Comparison with field data is provided, and a new model to compute fragmentation energy from particle size distribution is proposed

Supporting Information:
- Supporting Information S1

Correspondence to:
F. V. De Blasio,
fabio.deblasio@unimib.it

Citation:
De Blasio, F. V., Dattola, G., & Crosta, G. B. (2018). Extremely energetic rockfalls. *Journal of Geophysical Research: Earth Surface*, *123*, 2392–2421. https://doi.org/10.1029/2017JF004327

Received 20 APR 2017
Accepted 6 SEP 2018
Accepted article online 11 SEP 2018
Published online 8 OCT 2018

Extremely Energetic Rockfalls

Fabio Vittorio De Blasio[1], **Giuseppe Dattola**[1], **and Giovanni Battista Crosta**[1]

[1]Department of Earth and Environmental Sciences, Università degli Studi di Milano-Bicocca, Milan, Italy

Abstract Extremely energetic rockfalls (EERs) are defined here as rockfalls for which a combination of both large volume and free fall height of hundreds of meters results in energy larger than about 80 GJ released in a short time. Examples include several events worldwide. In contrast to low energy rockfalls where block disintegration is limited, in EERs the impact after free fall causes immediate release of energy much like an explosion. The resulting air blast can snap trees hundreds of meters ahead of the fall area. Pulverized rock at high speed can abrade vegetation in a process of sandblasting, and particles suspended by the blast and the subsequent debris cloud may travel farther than the impact zone, blanketing vast areas. Using published accounts and new data, we introduce physically based models formulated on analogies with explosions and explosive fragmentation to describe EERs. Results indicate that a portion of the initial potential energy of the block is spent in rock disintegration at impact (typically 0.2%–18%), while other sources of energy loss (air drag, seismic, sound, and ground deformation) are negligible; consequently, more than 80% of the potential energy is converted to kinetic energy of the fragmented block (ballistic projection, shock wave, sand blast, and dust cloud). We also propose simple estimates for the flow of the dust cloud associated with an EER and its long settling time. The areal extent of the affected zone is estimated from the energy balance and an empirical power law relationship.

1. Introduction

Rockfalls are common occurrences on mountain slopes. Because falling blocks usually proceed in leaps or roll atop talus or colluvial deposits where the loss of energy is significant, their kinetic energy at impact is much less than the total potential energy available from the point of instability except for some interactions along and at the toe of steep cliffs. Exceptional situations occur where unstable blocks suspended on the flanks of very steep mountain peaks may descend along extreme heights following free fall trajectories. Typical examples include valleys carved by glaciers or high mountain peaks where permafrost thawing is more effective and causes detachment of large unstable volumes (e.g., Ravanel & Deline, 2008; Noetzli et al., 2007). These are quite common conditions in alpine landscapes and frequent and sequential collapses have been recorded in the last century (Luethi et al., 2015). Upon impact with the terrain, an enormous amount of energy on the order of 10 MJ per cubic meter of rock may be instantaneously dissipated with devastating effects.

Part of the initial block potential energy is dissipated by air drag, seismic waves, and soil deformation (Wieczorek et al., 2000). The rest of the energy is used in the impact process, which causes an explosive energy release and the instantaneous comminution of the rocky material that is cast at high speed from the impact point. The particles accelerate the air at rest, producing a shock wave akin to an explosion. The overpressure of the shock wave and the dynamic pressure acquired by the ensuing wind are capable of uprooting trees and can affect infrastructure for several hundred meters ahead of the center of impact (Wieczorek et al., 2000). The particles resulting from the disintegration may hit trees and obstacles at very high speed, scouring them severely or penetrating deeply. Finally, the finest component of the fragments is capable of traveling as a turbulent suspension, hereafter referred to as dust cloud (Wieczorek et al., 2007). Because this dust cloud may blanket an area about 5–10 km^2 ahead of the rockfall with powder composed of rock fragments, it may cause a temporary darkness (Wieczorek et al., 2000) ranging from tens of minutes to several hours.

In our study, we refer to the kind of phenomenon described above as extremely energetic rockfall (EER). From a general viewpoint, the definition of an EER should embrace rockfall phenomena characterized by the following sequence: detachment, free fall, impact, fragmentation, pulverization, and air blast. Afterward, on a longer time scale (minutes to hours), a dense dust cloud is formed, which travels along the valley, finally depositing as a thick dust layer. We exclude major rock avalanches and Sturzstroms from our definition,

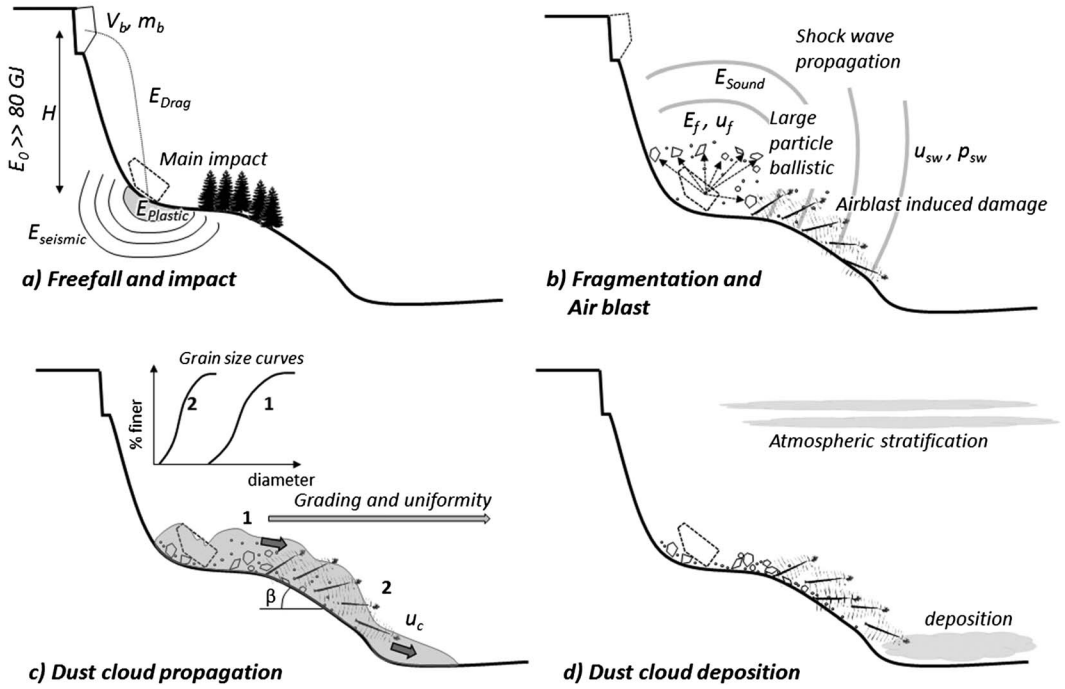

Figure 1. Schematic representation of the extremely energetic rockfall sequence from the original impact to the dust cloud stratification: (a) ballistic movement of the boulder of mass m_b and volume V_b with an initial potential energy E_0 and a drag energy dissipation E_{Drag} from the source area until the impact where the plastic soil dissipation E_{Plastic} and seismic dissipation E_{Seismic} take place; (b) fragmentation of the boulder with a fragmentation energy E_f and fragment velocity u_f and formation of the corresponding air blast characterized by a velocity u_{sw} and a pressure p_{sw}; (c) dust cloud propagation with a velocity u_c along the valley and a slope angle β; (d) deposition of the cloud.

characterized by long horizontal spread of the main mass compared to the vertical fall. We also exclude rockfalls characterized by block breakage into only a few large elements. We note that the EER phenomena may be considered as a subclass of cliff falls according to the nomenclature by Whalley (1974), characterized by high energetic content and volumes placing them at the boundary between cliff falls and Bergsturzs (in the sense of Whalley, 1974).

The 10 July 1996 rockfall at Happy Isles in Yosemite National Park (California, United States) was the first well-documented case of an EER (Wieczorek, 2002; Wieczorek et al., 2000; 2008). During the event, the rockfall traveled downward about 550 m and, after impact, extended over a horizontal length of more than 500 m, uprooting trees over an area of about 0.1 km^2. Unfortunately, such events are so unpredictable and rapid that they are first observed a few minutes after the initial triggering. Thus, images and videos often portray the event only during the development of the powdery cloud.

Figure 1 shows a schematic representation of the sequence of events commonly associated with an EER. Initially, a block of mass m_b detaches from a vertical wall and follows a ballistic trajectory (Figure 1a). Due to the high values of the vertical drop height and the block mass, the initial potential block energy E_0 is very high and the block impact is followed by a substantial and rapid fragmentation, ballistic projection of small fragments (fly rocks), and an air blast (Figure 1b). After the air blast is totally dissipated, a dust cloud travels along the valley, where selection and sorting of particles occur (Figure 1c) followed by deceleration and deposition (Figure 1d). During these last two steps, rocks and dust are deposited with a uniformity and mean size, which increase and decrease with distance, respectively.

Images during and immediately after rock fall impact, along with pertinent data of several EERs, illustrate the dramatic extent of these events (Figure 2 and Table 1). Note that the generation of air blasts and large dust clouds is not exclusive to EERs and has also been observed in most of the rock avalanches reported in the literature (e.g., Randa rockfall by Erismann & Abele, 2001; Thurwieser rock avalanche by Sosio et al., 2008; Brenva rock avalanche by Deline, 2001, Noetzli et al., 2006; and Val Pola rock avalanche by Crosta et al., 2004).

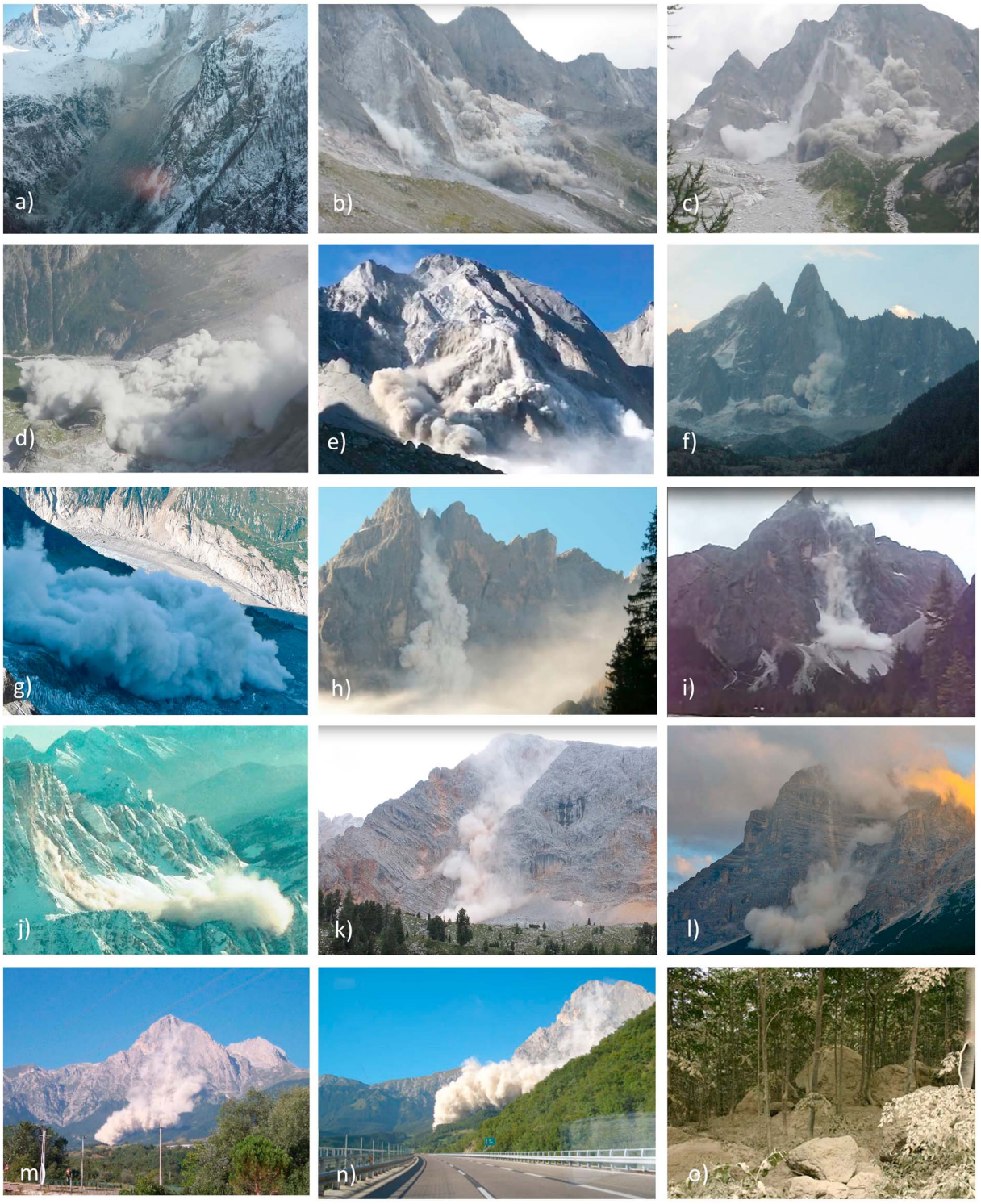

Figure 2. Examples of recent extremely energetic rockfalls. See Table 1 for details about the specific events Cengalo, 27 December 2011, ~1.5–2.0 · 10^6 m^3, M = 2.7, photo by M. Negrini; (b and c) Cengalo, 11 September 2016, ~150,000 m^3, from videos by R. Christoffel; (d) Cengalo, 21 August 2017, ~150,000 m^3 from video by R. Dujmovits M = 2.3; (e) Cengalo 23 August 2017, ~3.5·10^6 m^3, M = 3, from video by R. and B. Salis; (f and g) Dru 11 September 2011, ~43,000 m^3, photo by D. Taylor; (h) Cima Una Fiscalina 12 October 2007 M = 0.8; (i) Cima Una Fiscalina July 2012; (j) Monte Civetta 16 January 2013, 50,000 m^3; (k) Croda Rossa 18 August 2016, 500,000–700,000 m^3; (l) Monte Pelmo 29 July 2016, photo by S. Polloni, (m–o) Gran Sasso, 22 August 2006, photo by Giulio D'Agostino, Casamonteverde.

The aim of this paper is to provide preliminary analysis and criteria for estimation of the physical processes occurring during block fragmentation (ballistic projection, shock wave, sand blasting, and dust cloud propagation) and the effects on the surrounding area during EERs. We develop simple analytical formulations rather than numerical simulation. Even though comprehensive calculations should be specific to each case study, analytical approaches permit a direct application based only on inputs of energy and mass. We analyze field observations and laboratory results and apply the analytical formulations to three case studies for which varying levels of description are available. The extension and modification of the analytical formulations shown in this paper should make possible an estimation of the energy of past events and also predict the potential for air blast effects in future events.

2. Definition and Identification of EERs

2.1. Definition of EERs

We define EERs as those events in which the following three criteria are all met:

1. *High specific energy (or equivalently great fall height)*.The falling mass should travel along a ballistic trajectory for a height sufficient to disintegrate explosively at contact with the ground, producing some larger blocks and residual particles ranging from a few centimeters to micrometers.It is reasonable to expect that the degree of fragmentation increases progressively as a function of the fall height (Corominas et al., 2017; Crosta et al., 2015; Frattini et al., 2012). However, it is not possible to define unambiguously a threshold limit to an explosive fragmentation. Experimental work, usually limited to some tens of meters of fall (Giacomini et al., 2009), does not show the onset of explosive fragmentation that we wish to capture in our definition of EERs. However, in nature it is observed that impacts after falls of some few hundred meters have an explosive character (Wieczorek, 2002). For this reason, we define EERs as having a fall height greater than 300 m, which, for the case of a vertical fall and neglecting the air resistance, corresponds to a vertical velocity at impact of about 77 m/s $(=\sqrt{2g\cdot 300\mathrm{m}})$ and to an energy per unit mass of 2,943 J/kg ($=g\cdot 300$m).
2. *Large mass*. We restrict the definition of EER to rock volumes sufficiently large (on the order of 10,000 m^3 or more) to produce severe damage.
3. *Energy released at once*. The primary fragmentation event for a rock fall categorized in the definition of EER should not last longer than a few seconds. As a reference for time, we note that the travel time needed for a block of radius 50 m to travel along a distance equal to its diameter after 500 m of free fall is about 1 s.

Summarizing, our definition requires a rockfall mass carrying a total kinetic energy of at least 80 GJ, which is the energy released by a boulder of density 2,500 kg/m^3 and volume 10,000 m^3 falling from a height of 300 m. Most common rockfalls in which a boulder bounces and rolls to lower elevation as well as major rock avalanches are excluded from the present definition because they do not satisfy requirement (iii). The fulfillment of all three criteria identifies a unique kind of rockfall, that is, EER, in which a high amount of concentrated energy goes into prompt fragmentation and blast.

2.2. Disintegration Number

To better quantify the distinctive criteria of EERs, we have to take into account the amount of fragmentation produced during the impact. Therefore, it is necessary to identify a dimensionless number, here defined as the disintegration number (N_{dis}), which describes a criterion to evaluate the tendency for fragmentation.

It is known that rock fracture is due to crack propagation (Atkinson, 1987). Although it is possible, in principle, to calculate the dynamics and the energy required for the fragmentation starting from basic physical principles (using variables such as the fragmentation specific energy, Young's modulus, and interatomic distance), the complexity of this approach, complemented by the lack of complete or reliable data and descriptions, is too demanding for practical problems, and therefore, it is better to compute the fragmentation energy with empirical methods.

The block fracture energy has been defined as the energy per unit mass (averaged over many trials) at which a spherical object breaks upon falling (e.g., Andrews & Kim, 1998; King, 2001). Although the block fracture energy depends on the size of the particle (small particles are more resistant), it is possible to extrapolate an asymptotic value (E_{f2}/m_b) for very large clasts where E_{f2} is the fragmentation energy necessary to divide a particle in two clasts (King, 2001) and m_b is the block mass. Thus, E_{f2}/m_b represents the block fracture

Journal of Geophysical Research: Earth Surface

10.1029/2017JF004327

Table 1
Selected Examples of Extremely Energetic Rockfalls

Event #	Location and date	Volume (m^3) and rock type	Fall height (m) and motion description	Impact velocity (m/s) $(2gh)^{0.5}$	Impact energy (TJ)–(kilotons) (1 kt = 4.184 TJ)	Air response	References
1	Two events in Happy Isles, Yosemite National Park, California, United States (1996)	23,000 and 38,500 granite	650, of which 550 in free fall	104–113, most likely value 107	0.32–0.077	Winds at 110 m/s crashed and severely abraded trees;	Morrissey et al. (1999), Wieczorek et al. (2000), and Wieczorek (2002)
2	Ahwiyah Point, Yosemite National Park, California, United States (2009)	46,700 granite	730	120	0.86–0.20	Air blast knocked over trees 3.3 s after the impact and 50 m beyond the talus edge	Zimmer et al. (2012)
3	Paretone, Gran Sasso (Italy; 22 August 2006)	30,000 limestone	1,000; frequent collisions with the flank reduced impact velocity from theoretical free-fall value of 141 m/s	80	0.25–0.060	Uprooted and abraded trees; dust cloud reaching to the highway	Bianchi-Fasani et al. (2013) and Bianchi-Fasani et al. (2008)
4	Cima Una,Val Fiscalina (Italy; 12 October 2007; 2011)	2007: 40,000 2011: ~500 dolostone	900	133	0.987–0.236	Uprooted and abraded trees; dust cloud	Viero et al. (2013)
5	Les Drus (France; 12 events since 1905; the latest in 2011; from cliff toe to upper sectors)	1905: 9,000 1935–1940: 5,500 1950: 20,000 1977: 27,000 1997: $2*10^6$ 2003: 6,500 2005: 265,000 2011, 59,200 granite	500	99	0.870–0.208	Dust clouds	Ravanel and Deline (2008)
6	Nevados Huascaran (Peru; 1970)	7,000,000–100,000,000	600 (the first collapse onto the glacier (511); with the rock fragments continuing further for several kilometers)	78–200	400–2.6	Very strong shock wave (with concentric features on the glacier) followed by tree abrasion	Plafker and Ericksen (1978)
7	Croda Rossa (Dolomites, Italy, 19–20 June 2016; 18 August 2016)	600,000; carbonate 500,000–700,000 dolostone	1,000; the relatively gently sloping terrain reduced the speed; 500	140 99	16.50–3.94; 7.65–1.83	Massive dust cloud	—
8	Cengalo (2011, 2016, 2017, Switzerland)	2011: $1.5–2.0 \times 10^6$ 2016: 150,000, 2017: 4×10^6 quartzdiorite	~500	99	17.30–4.15	Massive high-speed dust cloud	—
9	Monte Civetta (2013, Italy)	50,000 dolostone	820; steep rocky cliff	127	1.05–0.25	Dust cloud	—
10	Monte Pelmo (2016, Italy)	dolostone	800	unknown	—	—	—
11	Mount Granier (2016, France)	(Multiple failures) larger than 100,000	700	117	1.85–0.44	Dust cloud	Ravanel et al. (2016)

Note. The impact energy is expressed also in kilotons (thousands of tons of TNT), a traditional unit of measure for explosions.

energy, that is, the energy per unit of mass necessary to break the large clast in two parts. For example, E_{f2}/m_b for limestone and quartz are respectively about 114 J/kg and 43.4 J/kg (King, 2001). Giacomini et al. (2009), studying a situation closer to the natural setting in which ton size gneissic boulders were dropped from heights varying between 20 and 40 m (196 and 392 J/kg), found that from this height only a few fragments are produced (1 to 22 in number). Fries (2013) performed experiments in gneiss rock and found a number of fragments ranging between 20 and 140 for a fall height around 50 m. For spheres of aluminum oxides, the threshold energy is about 800 J/kg (Andrews & Kim, 1998).

We define the dimensionless disintegration number as

$$N_{\mathrm{dis}} = \frac{\text{Blockenergy atimpact per unit of mass}}{\text{Fractuneenergy per unit mass}} = \frac{\frac{E_0}{m_b}}{\frac{E_{f2}}{m_b}} = \frac{E_0}{E_{f2}}, \tag{1}$$

which represents the ratio between the amount of energy available and the energy required for the fragmentation. The disintegration number for an EER is much larger than unity (e.g., $N_{\mathrm{dis}} \gg 46$ as obtained from back calculation of the case study values reported in Table 1), which implies a multifragmentation of the block.

Table 2 introduces a classification of rockfall events based on indicative values of the energy involved, the disintegration number, and the size of the smallest fragments. The common rockfall class represents fresse fall heights of tens of meters and is based on values reported by Giacomini et al. (2009), while the EER values are determined from the Table 1 case studies. For completeness, we introduce *intermediate* rockfalls as a transition class between common rockfalls and EERs. By increasing the energy involved, the disintegration number increases and clast size becomes smaller. This implies that during EERs, the energy available at impact is used to disintegrate the rock into more fragments than in common rockfalls, and of much smaller size (Zhao et al., 2017). The values shown in Table 2 are considered indicative of EERs.

3. Impact Study and Fragmentation

3.1. Large and Small Clasts Formed During an EER

Data (Viero et al., 2013; Wieczorek et al., 2007) show that during an EER, two populations of clasts are produced upon impact. Relatively large, centimeter-sized blocks to boulders up to few meters in diameter are partly deposited in the talus immediately beneath and downslope of the impact point, and partly are ejected at high speed. A second population of clasts is composed of sand to clay-sized rock (hereafter referred to as *powder*). These small grains are initially launched at very high speed away from the impact point and form a cloud of rock powder.

Crosta et al. (2007) and Hogan et al. (2012) found that the integral size distribution for grains produced during low-energy impact experiments against rock is well fitted by a power law whose exponent is the fractal dimension with a power spectrum of about 2 when the integral fraction is plotted as a function of the particle diameter. Gili et al. (2016) propose a similar power law with an exponent ranging between 0.18 and 0.69 for much larger clasts (between several centimeters to meters in diameter) that chip off boulders during artificial rock falls. However, the size range where these power law functions hold is never wider than 2–3 orders of magnitude in terms of clast diameter. If we apply these simple power law functions to the clasts of an EER (where clast diameters span 5–6 orders of magnitude), the single power law cannot describe the whole clast population with a single set of parameters due to the broad range of clast diameters.

Hogan et al. (2012) showed that the integral spectrum follows a power law distribution in which the integral particle fraction is inversely proportional to the squared particle diameter. However, such a relationship is not able to reproduce the range of particle diameters observed during an EER. Indeed, if this law is used, the resulting volume integral fraction for large clasts would be about 10^{10} smaller than the corresponding value for smaller clasts. This is in contradiction with the in situ results showing that the above ratio ranges between 10^{-2} and 10^{-3} (Wieczorek et al., 2000).

Thus, for practical reasons, these two populations of clasts will be considered separately. Fortunately, only the smallest particles contribute significantly to the total area created by fragmentation, and to the fragmentation energy as calculated in section 4. If we define η_v as the fraction of mass transformed to very small

Table 2
Proposed Classification of Rockfall Types as a Function of Energy Released, Disintegration Number, and Smallest Fragment Size

Variable	Common rockfalls (Giacomini et al., 2009)	Intermediate rockfalls	EER
Energy released (J/kg)	0–500	500–2,000	>2,000
Disintegration Number	0–12	12–46	> 46
Smallest fragment size (m)	0.2–1.0	0.004–1.0	<0.004

fragments (i.e., powder fragments), the mass to be used in the computation of the fragmentation energy is $\eta_v m_b$, while the remaining mass in the large size population is $(1 - \eta_v)m_b$.

3.2. Energy Balance

During an impact, the difference between the initial block potential energy of the block E_0 and the dissipated energy E_d is converted to the elastic strain energy that is stored by the block. If this energy overcomes a threshold given by fragmentation energy (E_f), fragmentation will occur. The difference between the stored energy and the fragmentation energy is the residual energy after the fragmentation, which will be converted into the kinetic energy of the fragments (E_{kf}).

Thus, the initial fragment kinetic energy is calculated from the following energy balance:

$$E_{kf} = (E_0 - E_d) - E_f. \tag{2}$$

The initial block potential energy of the block ($E_0 = m_b gH$) can easily be calculated from the initial elevation (H), the block mass (m_b), and gravitational acceleration (g), whereas E_d and E_f must be evaluated with specific models illustrated in the following sections. Furthermore, we define a coefficient of fragmentation efficiency $\eta = E_{kf}/E_0$ as the ratio of the kinetic energy of the fragments relative to the initial potential energy of the block.

3.3. Estimation of Energy Dissipation (E_d)

Bouncing and sliding along the upper slope may dissipate a certain fraction of the available energy, thus reducing the energy and the velocity. It is possible to evaluate the dissipation energy for cases when sliding and bouncing occur. However, in the following analysis we neglect sliding and bouncing that occur before the final block impact as we are more interested in the EER phenomena.

Different dissipation mechanisms take place during free fall and impact, which are related to the corresponding dissipated energy, namely, (i) air resistance, E_{Drag}; (ii) seismic waves, E_{Seismic}; (iii) sound, E_{Sound}; and (iv) plastic soil deformation, E_{Plastic}. In the following, we present formulations for each of these energy components individually.

3.3.1. Dissipation Due to Air Resistance (E_{drag})

The energy dissipated by air resistance is equal to the work done by the air drag force against which an EER rock mass is moving. The drag force acts on the cross section of the block (e.g., Hughes & Brighton, 1967) and, for very high Reynolds numbers, can be computed as $F_{\text{Drag}} = \frac{1}{2}\rho_{a,0} C_b A_b {u_b}^2$, where $\rho_{a,\,0}$ is the air density in standard conditions (1.225 kg/m^3 at 15 °C), C_b is the block air drag coefficient, A_b is the cross-sectional area of the block, and u_b the block velocity. The total energy dissipated by air resistance during a vertical fall is then

$$E_{\text{Drag}} = \int_0^H F_{\text{Drag}} \mathrm{d}z = \frac{1}{2}\rho_{a,0} C_b A_b \int_0^H u_b^2 \mathrm{d}z, \tag{3}$$

where z is the downward vertical coordinate (z = 0 m corresponds to the original position of the block). For simplicity, the boulder is assumed spherical and its cross section is $A_b = \pi R_b^2$. As a consequence of the drag force, during the block fall, the velocity increases to slightly less than the theoretical free fall velocity (Hughes & Brighton, 1967). In theory the drag force would bring a block to constant velocity (the limit velocity, u_b^{lim}) after a sufficient fall height. For very high Reynolds numbers ($>10^6$), a reasonable value for the block air drag coefficient C_b is between 0.5 and 1.0 (Hughes & Brighton, 1967). By imposing that the drag force with $C_b = 1$ is equal to the weight force for a block of $R_b \approx 10$m, we find that the limit velocity ranges between $u_b^{\text{lim}} \approx 832\text{m/s}$ (C_b = 1.0) and $u_b^{\text{lim}} \approx 1,177\text{m/s}$ (C_b = 0.5), which is much greater than the typical maximum impact velocity of

Table 3
Seismic Energy Computation for the Yosemite, Cengalo, and Cima Una Case Studies

Case study	E_0 (GJ)	M (−)	$E_{Seismic}$ (GJ)	$E_{Seismic}/E_0$
Yosemite-Happy Isles (1996)	322.65	2.15	5.64E−03	1.75E−05
Yosemite-Ahwiyah Point (2009)	936.41	2.40	1.68E−2	1.79E−5
Cengalo (2016)	1530	2.3	1.09E−02	7.11E−06
Cengalo (2017)	1530	3	2.16E−01	1.41E−04
Cima Una	918.2	0.8	1.20E−05	1.30E−08

Note. The seismic energy is computed by using equation (5) with k = 9.4, α = 2.14 and β = − 0.054.

EERs (see Table 1). We find the fall height necessary to reach a fraction α of the limit velocity is $H_{lim} = -\frac{4}{3}\frac{R\rho_s}{c_D\rho_a}\ln(1-\alpha)$, and using $\alpha = 0.1$, we find $H_{lim} \approx 4.6$km. Because the fall height of EERs is much less than the height necessary to achieve 10% of limit velocity, we can neglect the effect of air resistance in the block velocity and therefore we use the free fall velocity $u_{b,\max} = \sqrt{2gH}$ in equation (3). Using this velocity in the conversion of the potential energy to kinetic energy, and converting the radius (R_b) in terms of the particle volume (V_b) results in

$$E_{Drag} = \frac{1}{2}\rho_{a,0}C_bA_b\int_0^H(2gz)\mathrm{d}z = \frac{1}{2}\rho_{a,0}C_bA_bgH^2 = \frac{\pi}{2}\left(\frac{3}{4\pi}\right)^{\frac{2}{3}}V_b^{\frac{2}{3}}\rho_{a,0}C_bgH^2 = \left(\frac{9\pi}{128}\right)^{\frac{1}{3}}V_b^{\frac{2}{3}}\rho_{a,0}C_bgH^2. \quad (4)$$

By using again C_b in the range between 0.5 and 1.0, E_{Drag} will range between $2.97V_b^{\frac{2}{3}H^2}$ and $5.93\ V_b^{\frac{2}{3}H^2}$.

The ratio between the air-dissipated energy and the initial potential block energy (assuming ρ = 2,500 kg/m^3) ranges from $0.0012V_b^{-\frac{1}{3}}H$ to $0.0023V_b^{-\frac{1}{3}}H$, which is in every case negligible (less than 0.01), so that the air dissipated energy can be neglected.

3.3.2. Seismic Wave Dissipation ($E_{Seismic}$)

Seismic waves propagate in the soil from the impact point (e.g., Favreau et al., 2010; Gualtieri & Ekström, 2016; Morrissey et al., 1999; Wieczorek et al., 2000). The seismic energy released during a landslide or rockfall is considered to be a very small fraction of the total energy (Deparis et al., 2008; Morrissey et al., 1999; Zimmer et al., 2012). The standard relationship between magnitude M and the energy released during a seismic event is quantified by the Gutenberg-Richter law (1956):

$$\log E_{Seismic} = K + \alpha M + \beta M^2, \quad (5)$$

where K, α, and β are three empirical and typically regionally fit parameters. Here we use the standard values K = 9.4, α = 2.14, and β = − 0.054 reported by Gutenberg and Richter (1956), where E_s is expressed in ergs (1 erg = 10^{-7}J). By using equation (5) and the magnitude of two seismic events generated by rockfalls as reported in Wieczorek et al. (2000) and Zimmer et al. (2012), we find that the seismic energy involved is negligible compared with the initial potential energy of these rockfalls (i.e., 0.002% of E_0, Table 3). Deparis et al. (2008) reached the same conclusion using the equation proposed by Kanamori (1977) in place of the Gutenberg-Richter law. In addition, seismic data confirming the low value of seismic energy during rockfalls (a fraction on the order of $10^{-4} - 10^{-5}$) compared to potential energy have been published recently (Farin et al., 2015, 2018; Hibert et al., 2011, 2014; Lévy et al., 2015). Thus, it is possible to ignore $E_{Seismic}$ in the calculations of the dissipation energy.

3.3.3. Sound Dissipation (E_{Sound})

It is not easy to accurately estimate the sound dissipation of EERs due to a lack of reliable observations. Indeed, we did not find that available videos and eye witnesses accounts from reported EERs recorded noise as an important consequence. Thus, we assume that the highest noise intensity is likely to be much less than the human threshold for noise-induced discomfort and pain (taken to be 1 and 10 W/m^2, respectively, see Camp et al., 1962). Assuming that the sound propagates isotropically from the source, the sound energy moves along a hemisphere, its value is $E_{Sound} = e_{Sound}2\pi R^2\Delta t$, where e_{Sound} is the sound intensity, R is the radius of the semisphere, and Δt is the time interval when the sound propagates. Therefore, at a radius of

1,000 m (as an upper limit of the distance of observation in the videos in the supporting information) and considering a duration of sound waves of 10 s, which is likely an over estimate, we evaluate the total sound energy as $E_{\text{Sound}} \ll 1 \frac{W}{m^2}\ 2\pi\ (1,000\ \text{m})^2 (10\ \text{s}) = 63\ \text{MJ}$. This value appears negligible compared with other forms of energy involved so that in the next calculation we do not consider it.

3.3.4. Contact Pressure

To evaluate the plastic deformation energy of ground material at impact (E_{plastic}), it is important to derive the contact pressure ($p(t)$) between the block and soil. According to the impulse-momentum theorem, the impulse (i.e., time integral of the contact force) is equal to the variation of the momentum, and here we assume that the final velocity ($u_{b,f}$) approaches zero because, after impact, the block stops and disintegrates into fragments

$$\int_0^{t_I} A_b\ \mathrm{p}(t)\mathrm{d}t = \rho V_b \left(u_{b,\max} - u_{b,f}\right) = \rho V_b u_{b,\max}, \tag{6}$$

where t_I is the impact time. To simplify equation (6), we assume that (i) the impact pressure is constant in space and linear in time and (ii) the subsequent deceleration is constant. Despite their simplicity, these assumptions reasonably capture the salient behavior of rockfall impact processes for EERs.

Thus, from equation (6) the time-averaged value of the contact pressure is

$$p_{\text{mean}} = \frac{\rho V_b u_{b.\max}}{A_b \mathrm{t_I}}. \tag{7}$$

At the end of the impact and before disintegration, the block can be considered totally deformed so that the impact time t_I is very short and can be approximated as $t_I = 2R_b/u_{b,\max}$.

Substituting t_I into equation (6), the following estimation of the contact pressure is obtained

$$p_{\text{mean}} = \frac{\rho V_b u_{b,\max}^2}{2A_b R_b}\ . \tag{8}$$

If we assume a spherical block and neglect air resistance (i.e., $u_{b,\max} = \sqrt{2gH}$) then (8) becomes

$$p_{\text{mean}} = \frac{\rho V_b u_{b,\max}^2}{2A_b R_b} = \frac{\frac{4}{3}\rho\pi R_b^3\ u_{b,\max}^2}{2\pi R_b^2 R_b} = \frac{2}{3}\rho u_{b,\max}^2 = \frac{4}{3}\rho g H. \tag{9}$$

Equation (9) predicts fairly well the average pressure developed by large spheres impacting against walls in experimental settings (Hofmann & Molk, 2012; Lambert et al., 2014).

3.3.5. Plastic Deformation Energy of Ground Material (E_{Plastic})

Our formulation to estimate plastic deformation energy of ground material makes the following simplifications: (i) the soil medium is a continuum, (ii) the constitutive model is rigid plastic, and (iii) only a radial strain field develops during the impact so that only volumetric effects contribute to the dissipation. According to these assumptions, the energy dissipated by plastic soil deformation is

$$E_{\text{Plastic}} = p_{\text{mean}}\ \Delta V_s, \tag{10}$$

where ΔV_s is the change in volume of the ground material undergoing plastic deformation (i.e., equal to the volume of the generated crater), which should be measured in the field taking into account that some debris may fill the crater.

If we consider, for the sake of simplicity, a cylindrical crater of height H_s and radius equal to block radius, equation (10) becomes

$$E_{\text{Plastic}} = \left(\frac{4}{3}\rho g H\right)\left(\pi H_s R_b^2\right) = m_b g H \frac{H_s}{R_b} = E_0 \frac{H_s}{R_b}, \tag{11}$$

Since from in situ evidence we observed that the H_s/R_b ratio is small, then E_{Plastic} can be neglected and this becomes more evident for impacts on rock ledges.

3.4. Areal Extent of Fragmented Particles and Fragmentation Energy (S_f, E_f)

3.4.1. Areal Extent of Fragmented Particles

The fragmentation process consists of breaking the rock mass into much smaller clasts, which will deposit on the surrounding area. Here we calculate the corresponding areal extent of fragmented particles.

The surface area of fragmented particles is equal to

$$S_f = \int_{D_m}^{D_M} \mathrm{d}S_f(D), \tag{12}$$

where $\mathrm{d}S_f(D)$ is the elementary surface due to particles of diameter D integrated over the range of minimum (D_m) and maximum (D_M) fragment sizes. If the cumulative grain size distribution ($P(D)$, see supporting information) is known, then the elementary surface is the product of the number of newly created fragments ($\frac{\mathrm{d}P}{\mathrm{d}D}dD$) and the surface area of each fragment $\frac{\pi}{\psi}D^2$, which is to say

$$\mathrm{d}S_f(\mathrm{D}) = \frac{\pi}{\psi}\frac{\mathrm{d}P}{\mathrm{d}D}D^2\mathrm{dD}, \tag{13}$$

where ψ is the sphericity index (Rhodes, 1998), that is, the ratio of the surface area of a sphere having the clast volume, and the actual clast area ($\psi = 1$ for the spherical clasts).

Substituting equation (13) into equation (12) the areal extent of fragmented particles is

$$S_f = \frac{\pi}{\psi}\int_{\mathrm{D_m}}^{D_M}\frac{\mathrm{d}P}{\mathrm{d}D}D^2\mathrm{d}D. \tag{14}$$

Note that the special case of the uniform size fragments can be obtained by setting the derivative of cumulative distribution proportional to the Dirac delta function ($\frac{\mathrm{d}P}{\mathrm{d}D} \propto \frac{V_b}{D^3}\delta(D-\overline{D})$) in equation (14). This case can also be derived directly to show the dependency of the generated surface area from clast size. Let us consider a mass of diameter $2R_b$, which is fragmented into uniform sized particles of diameter D and volume $\propto D^3$. Under the condition that particles do not superpose and the areal extent of fragmented particles is the sum of the surface area of each particle, the created surface is the product of the number of newly created fragments ($\propto \frac{V_b}{D^3}$) and the surface area of each fragment ($\propto D^2$) such that $S_f \propto \frac{V_b}{D}$. It follows that the areal extent of fragmented particles is inversely proportional to the particle size ($\propto \frac{1}{D}$). This means that small particles have more influence on the created area. Despite the simplicity of this argument derived from a uniform particle distribution, the inverse dependence of surface area on the fragment size is valid in a general sense.

3.4.2. Fragmentation Energy

Since a large amount of area is created by fragmentation, a considerable amount of energy must be used in breaking the bonds within the rock. This energy, here referred to as the fragmentation energy, critically controls the newly created surface area of the fragmented rock mass (Crosta et al., 2007; Hogan et al., 2012). Therefore, we propose to quantitatively derive the fragmentation energy from the newly generated surface.

Generally speaking, the fragmentation specific energy depends on many factors such as the particle size compared to the crystal size or clast orientation with respect to cleavage. In the literature, the fragmentation energy is computed by employing simplified empirical strategies. Some authors (Crosta et al., 2007; Davies & McSaveney, 1999; De Blasio, 2005; De Blasio & Crosta, 2014; Locat et al., 2006) compute the fragmentation energy by means of a proportionality power law according to the approach proposed by Bond (1952). Rhodes (1998) reported that the expression by Bond (1952) is inappropriate for very small particles because it overestimates the fracture energy as discussed in De Blasio and Crosta (2016). Kick (1885) suggested a sort of scale invariance in the fragmentation energy so that the fragmentation specific energy is independent of particle size. von Rittinger (1867) proposed that the fracture energy is proportional to the surface area created by the process. However, approaches proposed by Kick (1885) and von Rittinger (1867) do not use the entire particle size spectrum and adopt an approximated expression based on one representative clast size only. In our work, we compute the fragmentation energy as

$$E_f = \int_{\mathrm{D_m}}^{\mathrm{D_M}}\mathrm{d}E_f = \int_{\mathrm{D_m}}^{\mathrm{D_M}}\gamma(D)\mathrm{d}S_f, \tag{15}$$

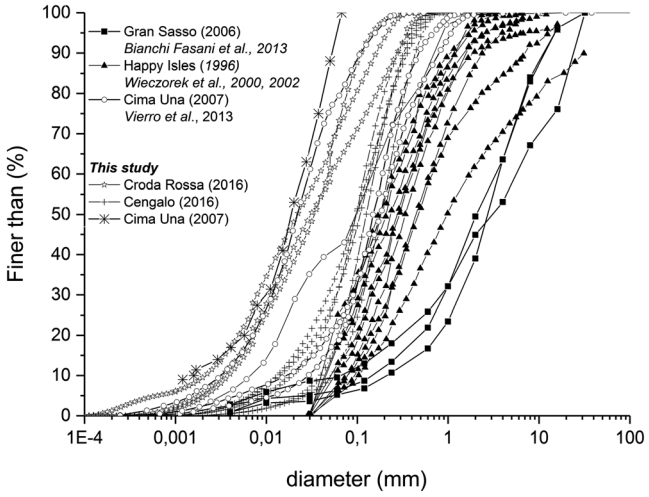

Figure 3. Grain size curves for fine dust samples from the literature and samples collected for this study. The uniformity coefficient $C_U = D_{60}/D_{10}$ ranges between 5.0 and 16.8 for the Happy Isles extremely energetic rockfall (EER; 1996), from 4.8 to 9.5 for the Cengalo EER (2016), and from 9.1 to 9.5 for the Cima Una EER (2007).

where dE_f is the elementary fragmentation energy, that is, the energy used to generate a surface equal to dS_f and $\gamma(D)$ is the fragmentation specific energy as a function of particle diameter. Equation (15) takes into account the entire spectrum of particles. The approximation where the fragmentation specific energy is scale invariant ($\gamma(D) = \gamma_0$) is a special case for which the fragmentation energy becomes:

$$E_f = \gamma_0 \int_{D_m}^{D_M} dS_f = \gamma_0 S_f. \quad (16)$$

Therefore, our model is a generalization of the model by Kick (1885). The values of γ_0 are reported by Tromans and Meech (2004) and Valero et al. (2011) for various types of rocks.

Since experimental observations demonstrate that the surface energies depend on many factors such as the rate of deformation (Grady & Kipp, 1987; Zhao et al., 2017), the stress distribution in the original body after the impact, and the fragment size, then the definition of an expression capable of representing the evolution of the fragmentation specific energy with the diameter could provide a more general framework. Following the observation of a scale dependency of strength on block size (Bieniawski, 1977; McDowell & Bolton, 1998; Weiss et al., 2014), we introduce a power law function $\gamma(D) = \gamma_0 \left(\frac{D_0}{D}\right)^{\alpha}$ characterized by a parameter α influencing the rate of fragmentation specific energy decay, and a representative diameter D_0 where the surface density of fragmentation energy is known (γ_0). While parameters D_0 and γ_0 have a well-defined physical meaning, α is empirical and should be calibrated by some experimental data. It should be stressed that this introduces more parameters compared to the simple approximation of fracture energy independent of size in equation (16).

By using the power law function for the fragmentation specific energy, and substituting equation (13) into equation (15), the fragmentation energy becomes

$$E_f = \int_{D_m}^{D_M} \gamma_0 \left(\frac{D_0}{D}\right)^{\alpha} dS_f = \int_{D_m}^{D_M} \gamma_0 \left(\frac{D_0}{D}\right)^{\alpha} \frac{\pi}{\psi} \frac{dP}{dD} D^2 dD. \quad (17)$$

For the scale-independent process ($\alpha = 0$), equation (16) is reobtained from equation (17).

3.5. Proposed Expressions for the Particle Size Distribution

To use Equations (14) and (17), it is necessary to have a mathematical expression for $P(D)$. We shall introduce analytical expressions fitting the experimental grain size distributions rather than experimental data themselves. In this way (i) we can compare our data with different expressions proposed in literature and (ii) in some cases the integrals can be computed in closed form.

We first analyze the particle size distribution resulting from explosive fragmentation by defining a series of analytical expressions. Figure 3 shows a collection of grain size curves for the finest EER-generated clasts from different sources. Examples of the geometry of clasts produced during the collapse of Cengalo and Cima Una EERs are shown in Figure 4. Notice the very small size and the shape that appear to be controlled by preexisting (e.g., cleavage) surfaces. By means of scanning electron microscope (SEM) analyses on samples from different sites (Cengalo, Cima Una), we were able to observe clasts composed of a single mineral species. For example, for quartz diorite of Cengalo submillimeter clasts are found (Figure 4), while typical crystal sizes of the original rock are millimetric to centimetric. Thus, the size of clasts is smaller than the original crystal size in the parent rock. Note the angularity of the produced clasts which implies large area per unit volume compared to the ideal case of cubic or spherical particles. Considering only the small clast population, typically, the smallest clasts range between 10^{-4} and 0.03 mm, and the largest surviving ones are in the 1–20 mm range (Viero et al., 2013; Wieczorek et al., 2000).

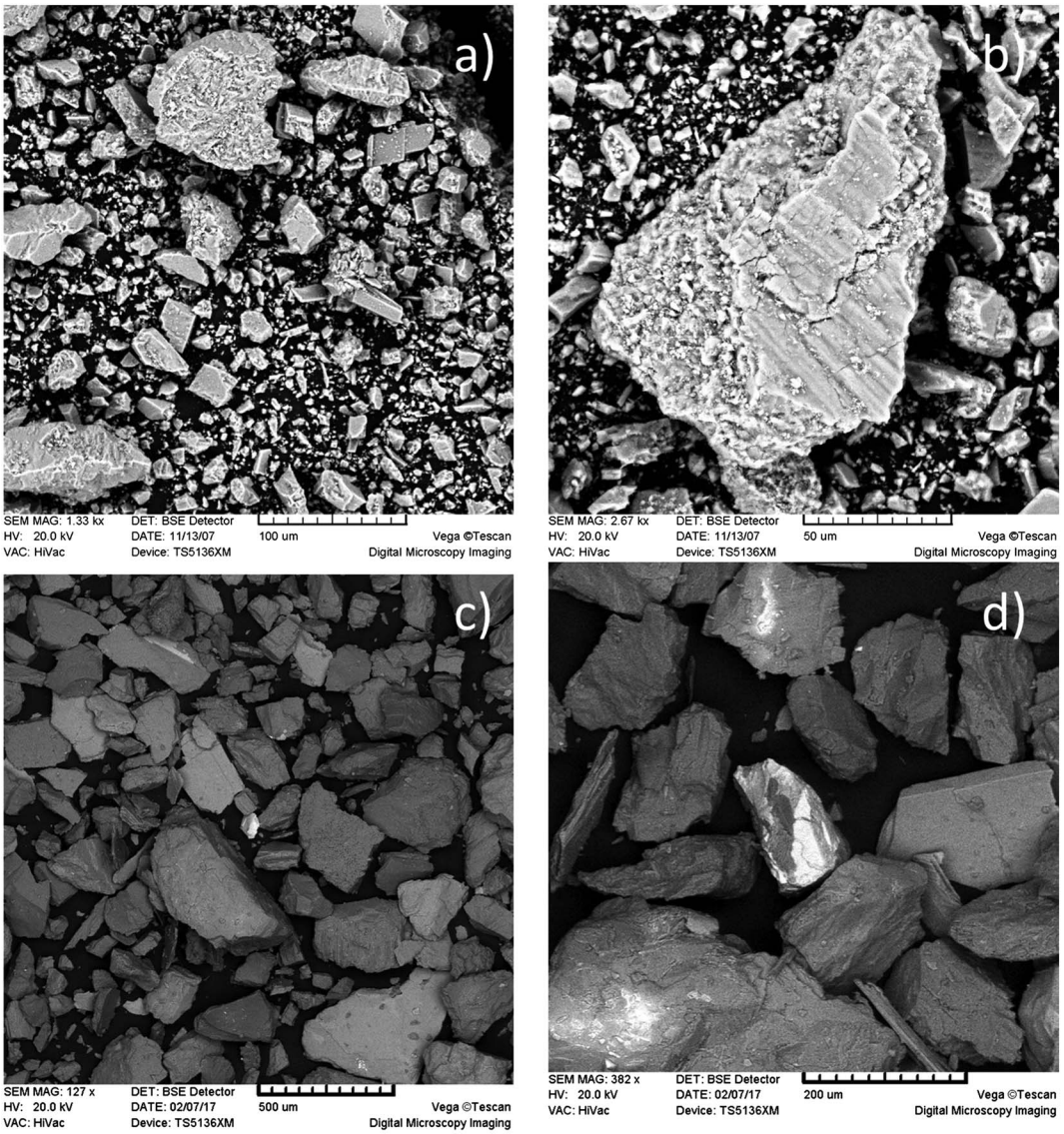

Figure 4. Scanning electron microscope images of fine powder samples collected at (a) and (b) the Cima Una extremely energetic rockfall site, in dolostones, and (c) and (d) the Pizzo Cengalo extremely energetic rockfall site, in granodioritic rocks. In all images, sharp failures are visible, with grain size comparable to crystal size of the original rocks.

In the following, we define the grain size distribution $G(D)$ as the percentage by weight of material with a diameter less than D. We investigate four grain size distribution functions: the homographic (proposed here), the Weibull (initially used by Rosin, 1933; Rosin & Rammler, 1933), the generalized extreme value (GEV), and the log normal.

The homographic curve is given by the expression

$$G(D) = \frac{a\,D + b}{cD + d}\ , \tag{18}$$

where c and d are two fitting parameters, whereas $a = a(c, d)$ and $b = b(c, d)$ are two functions obtained by imposing the following conditions

$$G(D_m) = \frac{aD_m + b}{cD_m + d} = G_m, \tag{19}$$

$$G(D_M) = \frac{aD_M + b}{cD_M + d} = G_M, \tag{20}$$

where G_m and G_M are the distribution values of the minimum (D_m) and maximum (D_M) fragment diameters, respectively (see supporting information).

The mathematical expression for the Weibull distribution is

$$G(\mathrm{D}) = \exp\left[-\left(\frac{D}{D_M\lambda}\right)^k\right], \tag{21}$$

where λ and k are two parameters to be calibrated against the experimental data. GEV expression is

$$G(\mathrm{D}) = \frac{(G_M - G_m)g(D) - G_m g(D_M)}{g(D_M)}, \tag{22}$$

being the function $g(D)$ given by

$$g(D) = \exp\left[-\left(1+\xi\left(\frac{D-\mu}{\sigma}\right)\right)^{\frac{1}{\xi}}\right] - \exp\left[-\left(1+\xi\left(\frac{D_m-\mu}{\sigma}\right)\right)^{\frac{1}{\xi}}\right], \tag{23}$$

where ξ is a shape parameter, σ is a scale parameter, and μ is a shift parameter all to be calibrated against experimental data.

Finally, the passing weight percentage obtained by lognormal distribution is calculated as

$$G(\mathrm{D}) = \int_{\infty}^{D} \frac{1}{\sigma'\sqrt{2\pi}} \exp\left(-\frac{\left(\ln D - \mu'\right)^2}{2\,\sigma'^2}\right) \mathrm{d}D\,, \tag{24}$$

where μ' and σ' are mean and standard deviation obtained from the experimental data. In the case of the homographic function (18), the areal extent of fragmented particles can be analytically computed in a closed form substituting the homographic function distribution into equation (14). The complete algebraic derivation is illustrated in the supporting information. The result of this mathematical manipulation is

$$S_f = -\frac{\pi}{\psi}\int_{D_m}^{D_M} \frac{6\eta_v V_b(ad-bc)}{\pi D^3(cD+d)^2} D^2 \mathrm{d}D = -\frac{6\eta_v V_b(ad-bc)}{\psi}\int_{D_m}^{D_M} \frac{1}{D(cD+d)^2}\mathrm{d}D, \tag{25}$$

where a coefficient η_v represents the part of the block volume that underwent fragmentation. Integration of equation (25) gives (see supporting information)

$$\begin{aligned} S_f &= -\frac{6\eta_v V_b(ad-bc)}{\psi}\int_{D_m}^{D_M} \frac{1}{D(cD+d)^2 ***}\mathrm{d}D \\ &= -\frac{6\eta_v V_b(ad-bc)}{\psi}\int_{D_m}^{D_M}\left[\frac{1}{d^2 D} - \frac{c}{d^2(cD+d)} - \frac{c}{d(cD+d)^2}\right]dD \\ &= -\frac{6\eta_v V_b(ad-bc)}{\psi}\left[\frac{1}{d^2}\ln\left(\frac{D_M}{D_m}\right) - \frac{1}{d^2}\ln\left(\frac{cD_M+d}{cD_m+d}\right) - \frac{1}{d}\left(\frac{1}{cD_M+d} - \frac{1}{cD_m+d}\right)\right], \end{aligned} \tag{26}$$

For the case of the Weibull distribution, the spectrum is

$$\frac{\mathrm{d}P}{\mathrm{d}D} = -\frac{6\eta_v V_b}{\pi D^3}\frac{\mathrm{d}G}{\mathrm{d}D} = \frac{6\eta_v V_b}{\pi D^3}\frac{k}{\lambda}\exp\left[-\left(\frac{D}{\lambda}\right)^k\right]\left(\frac{D}{\lambda}\right)^{k-1}, \tag{27}$$

so that the areal extent of the fragmented particles becomes

$$S_f = \frac{6\eta_v V_b}{\psi}\frac{k}{\lambda}\int_{D_m}^{D_M}\frac{1}{D}\exp\left[-\left(\frac{D}{\lambda}\right)^k\right]\left(\frac{D}{\lambda}\right)^{k-1}\mathrm{d}D, \tag{28}$$

The above integral does not have a closed form expression, so it has to be numerically computed.

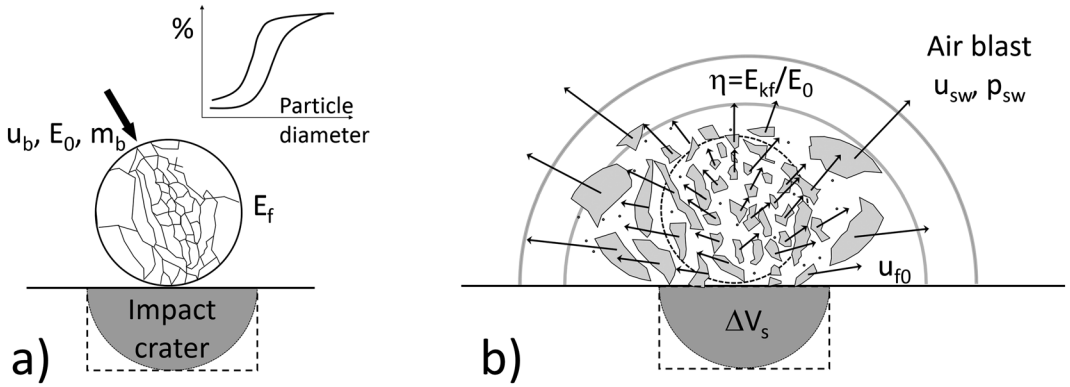

Figure 5. (a) Schematic representation of the clasts and impact crater at incipient fragmentation; (b) assumed clast movement (radially horizontal) and parameters involved (u_{sw} is the shock wave velocity, and $p_{sw}$is the shock wave pressure).

In a similar way, we calculate the expression for the areal extent of the fragmented particles for the GEV and the lognormal distributions

$$S_f = \frac{6\eta_v V_b}{\psi\sigma}\int_{D_m}^{D_M}\frac{1}{\xi}\left(1+\frac{\xi D}{\mu}\right)^{-\frac{1}{\xi}-1}\exp\left[-\left(1+\frac{\xi D}{\mu}\right)^{-\frac{1}{\xi}}\right]dD, \tag{29}$$

$$S_f = \frac{6\eta_v}{\psi\sigma'\sqrt{2\pi}}\int_{D_m}^{D_M}\frac{1}{D^3}\exp\left\{-\frac{\left(\ln D-\mu'\right)^2}{2\sigma'^2}\right\}dD\,. \tag{30}$$

In section 5, we apply these equations to EERs for which the granulometric curves are available.

4. Postimpact Phenomena

As anticipated, while the small clasts are suspended, large clasts either stop at the impact point or follow ballistic dynamics (i.e., so-called flyrock). Understanding the mobility of large clasts is especially important for assessing risk, as such clasts may represent a direct threat to people and infrastructures.

4.1. Distance Reached by Large Clasts

For design of protection measures, it is important to estimate the travel distance of the large clasts produced at block impact. Here we introduce a model in which a spherical EER block disintegrates into spherical clasts. We assume that at the initial condition just after the impact, each clast only has a spatially radial velocity component that, at incipient fragmentation (Figure 5), is equal to

$$\vec{u}_{f0} = u_{f0,\max}\,\frac{r}{R_b}\hat{r}, \tag{31}$$

where the initial clast velocity after the impact ($\vec{u}_{f0}$) parallel to the radial unit vector ($\hat{r}$) varies as a function of radial distance (r) from the center of the block to its full radius (R_b), such that fragments at the outer edge of the block ($r/R_b = 1$) have maximum initial velocity ($u_{f0,\ \max}$). Although fragment velocity should also depend on particle size, we do not know how velocity is distributed as a function of particle mass, so we assume the same velocity for all fragments at a given radius. Assuming that a fraction η_f of the initial kinetic energy E_{kf} is absorbed by the clast, the kinetic energy of the system can be obtained by summing the kinetic energy over all fragments, which when combined with equation (31) yields

$$\eta_f E_{kf} = \frac{1}{2}\left[\frac{1}{2}\int_{(1-\eta_v)V_b}\rho\left|\vec{u}_{f0}\right|^2 dV\right] = \rho\, u_{f0,\max}^2\frac{1}{4}\int_{(1-\eta_v)V_b}\left(\frac{r}{R_b}\right)^2 dV = \frac{3}{20}\rho(1-\eta_v)V_b\, u_{f0,\max}^2\,, \tag{32}$$

The first factor 1/2 follows from the fact that the disintegration of the block covers a hemispherical zone, while the second one is derived from the kinetic energy expression. By using the coefficient of fragmentation efficiency (η) in equation (32), the following relation is obtained

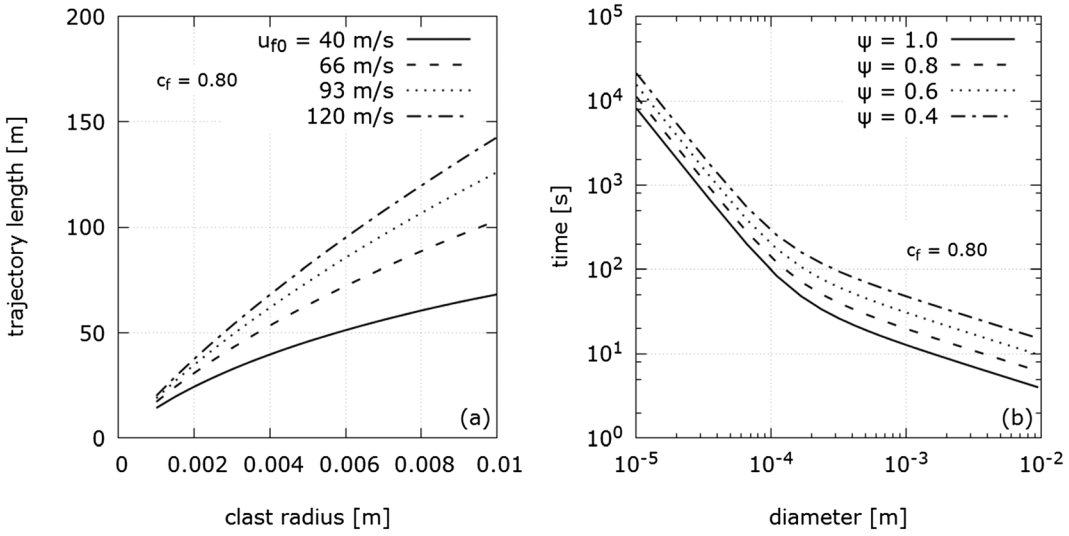

Figure 6. (a) Length of the ballistic trajectories calculated numerically as a function of the initial velocity (u_{f0}) and the clast radius for a fixed drag coefficient ($C_f = 0.80$, see equation (35)); (b) settling time for particles of different diameter and different shape coefficients (ψ) for a 100 m fall computed using the approach of Rhodes (1998).

$$\frac{3}{20}\rho(1-\eta_v)V_b\, u_{f0,\max}^2 = \eta_f E_{kf} = \eta_f \eta E_0 = \eta_f \eta\, \rho g H V_b, \tag{33}$$

so that the initial velocity of the fastest clasts is:

$$u_{f0,\max} = \sqrt{\frac{20}{3}\,\frac{\eta\eta_f g H}{1-\eta_v}}. \tag{34}$$

The initial clast velocity is calculated from equations (34) and (31), while the distance reached by the clast must be derived by the equation of motion. Without considering the interaction between clasts, the motion of each clast is governed by the gravity force and the air drag force that decelerates it

$$m_f \frac{d\vec{u_f}}{dt} = -\frac{1}{2} C_f\, A_f\, \rho_{a,0}\, |\vec{u_f}|\, \vec{u_f} - m_f \vec{g}, \tag{35}$$

where C_f is the air drag coefficient associated with the clast, A_f is the cross-sectional area of the clast, and $\vec{u_f}$ is the fragment velocity vector whose initial value is $\vec{u}_{f0}$. Because m_f is proportional to the clast volume, the final run-out depends on the fragment radius R_f. In equation (35) we used a different symbol for the air drag coefficient as in principle it differs from that of the block C_b in equation (4) due to the different Reynolds number and different shape. Equation (35) cannot be solved analytically and requires a numerical solution.

Figure 6a illustrates the results of a parametric analysis numerically calculated from equation (35) in which the drag coefficient is set to 0.8 (Hughes & Brighton, 1967). The length of the ballistic trajectories is shown for clasts with initial trajectory angle of 45° with respect to the horizontal plane and rock density $\rho = 2{,}700$ kg/m^3 considering different values of the initial velocities u_{f0}. In the analysis, the clast radius ranges from 0.001 to 0.01 m. Since the clast kinetic energy is proportional to R_f^3 and the drag force is proportional to R_f^2, the effects due to the drag force diminish with respect to the effect of the initial kinetic energy as the radius of the clast increases. Therefore, by increasing the clast radius, the trajectory length increases. Moreover, by increasing the radius the absolute value of the velocity at the ground approximately reaches an asymptotic value, which depends on the initial clast velocity. From Figure 6a, the maximum run-out observed is around 150 m for the assigned velocity.

4.2. Excess Pressure and Shock Velocity

After fragmentation, the residual energy and momentum of the smaller clasts are transferred to the air. According to Morrissey et al. (1999), the velocity of the particles in air exceeds the sound velocity (~343 m/s)

Table 4
Data of the Shock Waves Calculated for the Happy Isles Event Assuming $\eta_f = 0$

Variable	Values		
Distance r_{sw} (m)	100	400	1,000
Peak overpressure p_r (MPa)	0.13	0.010	0.005
Speed of shock wave/sound velocity u_{sw}/C_s (equation (36))	1.45	1.041	1.021
Wind velocity/sound velocity u_a/C_s (equation (37))	0.63	0.067	0.034
Air density/air density in standard condition $\frac{\rho_a}{\rho_{a,0}}$ (dust excluded; equation (38))	1.77	1.070	1.035

and consequently a shock wave is generated. This shock wave creates a wind capable of carrying smaller fragments, which are responsible for the observed abrasive effect on vegetation. In this section, the computation of the shock wave velocity and the corresponding excess pressure, as well as the velocity of the wind and its corresponding pressure, is presented.

The air blast process is akin to an explosion (Glasstone & Dolan, 1977), albeit with much lower energy per unit mass. By assuming that the smallest clast velocity is greater than the speed of sound, the shock wave velocity u_{sw} is given by (Glasstone & Dolan, 1977)

$$u_{sw} = C_s\left(1 + \frac{\Gamma+1}{2\Gamma}\frac{p_{sw}}{p_{a,0}}\right)^{1/2} = C_s\left(1 + 0.857\frac{p_{sw}}{p_{a,0}}\right)^{\frac{1}{2}}, \tag{36}$$

where Γ, p_{sw}, and $p_{a,\,0}$ are, respectively, the adiabatic coefficient of air (Γ = 1.4), the peak overpressure (i.e., the increment of air pressure at the shock wave front, which is at the origin of the air blast) and the standard air pressure, and C_s is the speed of sound. During its movement, the shock wave reduces its effects because the p_{sw} decreases as a function of the distance from the source point r_{sw}. In order to evaluate p_{sw}, we use the fitting suggested by Glasstone and Dolan (1977) for nuclear explosions, which correlates r_{sw} with the initial energy of the explosion without distinguishing between the different forms of energy associated with the clast distribution. So in our case $(1 - \eta_f)E_{kf}$ should be identified as the initial energy of the explosion.

Figure 3.72 of Glasstone and Dolan (1977) shows the value of p_{sw} as a function of r_{sw} for an explosion energy of 1 kt. In our calculation, the value of p_{sw} is obtained from their figure using a value of r_{sw} rescaled by a factor $\left(\frac{(1-\eta_f)E_{kf}}{1\text{ kt}}\right)^{\frac{1}{3}}$ to take into account energies different from 1 kt. This rescaling procedure is indicated by Glasstone and Dolan (1977). Once the p_{sw} is calculated, it is possible to compute the air velocity generated behind the shock wave at its peak as (Glasstone & Dolan, 1977)

$$u_a = \frac{5}{7}C_s\left(\frac{p_{sw}}{p_{a,0}}\right)\left(1 + \frac{6}{7}\frac{p_{sw}}{p_{a,0}}\right)^{-1}. \tag{37}$$

Due to the shock wave, the air density ρ_a increases as

$$\rho_a = \rho_{a,0}\left(1 + \frac{6}{7}\frac{p_{sw}}{p_{a,0}}\right)\left(1 + \frac{1}{7}\frac{p_{sw}}{p_{a,0}}\right)^{-1}. \tag{38}$$

During its propagation, this wind hits objects located at at distance r_{sw}, generating an overpressure whose peak value is (Glasstone & Dolan, 1977)

$$p_r = \rho_a u_a^2\left(p_{a,0} + \frac{4}{7p_{sw}}\right)\left(p_{a,0} + \frac{1}{7p_{sw}}\right)^{-1}. \tag{39}$$

Table 4 shows the value of peak overpressure, the ratio between shock wave and sound velocities, the ratio between air and sound velocities, and the ratio of the air density and air density in standard condition (i.e., the air density at temperature of 0 °C and at pressure of 1 bar) for the case of Happy Isles at three distances from the impact point. It is evident that all the relevant quantities decrease with increasing distance from impact point.

4.3. Sand Blast and Abrasive Wear

The mechanisms responsible for sand blasting during an EER are not well known, despite the abrasive effects on vegetation being amongst the most evident consequences of such phenomena (Bianchi-Fasani et al., 2013, 2008; Morrissey et al., 1999; Viero et al., 2013; Wieczorek et al., 2000; Wieczorek, 2002). In many ways,

the effect is analogous to industrial sand blasting used to polish surfaces. In sand blasting, pressures in the nozzle typically reach values on the order 1 MPa, and depending on design and other operation parameters, sand velocities may reach 450 m/s (Gorlach, 2011). In this section, we carry out a simple calculation of the velocity acquired by powder-sized particles during an EER.

During sand blasting, the air dynamic pressure is correlated with the particle velocity (Gorlach, 2011). In particular, the particle velocity used for blasting is about half the corresponding air velocity. In this framework, the maximum sand particle velocity $u_{a,\ \max}$ is assumed to be related to the dynamic pressure by the Bernoulli equation

$$P_{\text{dyn}} = \frac{1}{2}\rho_{\text{a}} u_{a,\max}^2, \tag{40}$$

where ρ_a is the air density, which is in principle different from $\rho_{a,\ 0}$, as the propagation of the shock front is compressed. Using P_{dyn} equal to 1 MPa as an upper limit for sand blasting (Gorlach, 2011), it is found that particle velocity is about 0.5 km/s. This high velocity combined with high sand particle flux intensity could explain the severity and persistence of abrasion also at relatively long distances from the impact point. Moreover, the angularity of fine particles, as shown in the SEM images of Figure 4, contributes to abrasion during the sand blasting of an EER. Indeed, the industrial applications of sand blasting for lower pressures (0.2 MPa is a more realistic value for a hand held nozzle) demonstrate that a very short time of less than 1 s is sufficient for effective paint removal.

4.4. Cloud Propagation

The available videos of EER events (supporting information) show that many powder-sized clasts form a dust cloud that moves along the slope similar to a powder snow avalanche. Although no direct lethal consequences of the dust cloud have been reported, a lofty cloud may reduce visibility and negatively affect local traffic and cause respiratory problems. Moreover, the subsequent reestablishment of normal activities and helicopter-assisted rescues may also be negatively affected. Thus, it may be useful to estimate the distance to which the dust cloud extends and the time of settling of powder-sized clasts. We emphasize that although we shall be exploring the cloud behavior generated by EERs, our consideration will be applicable to rock avalanche dust clouds as well.

Particulate clouds from EERs are initially set in motion partly by shear stress transmitted to the air by the exploding rock mass and debris. Over time, the subsequent acceleration is driven by the density difference between the suspended material and ambient air. After the acceleration phase, the cloud asymptotically reaches a state in which the gravity pull approximately equals the drag force, which results in decreasing velocity. In the simple model suggested here, the cloud has a thickness h_c, which is much smaller than its length, l_c, and width w_c,and it is assumed that the main flow occurs along the direction parallel to its length l_c. In our model, we assume that particle dispersion and differences in density within the cloud are neglected during motion, while lateral flows are taken into account updating the cloud width. Furthermore, we assume that the cloud moves along a slope with a constant inclination and that the differences between the behavior of the cloud front and body are not considered (Bridge & Demicco, 2008; Simpson, 1982). In this framework, the acceleration of the cloud can be written as the sum of a gravity acceleration term, and a drag frictional term in the following way

$$\frac{du_c}{dt} = \frac{\rho_c - \rho_{\text{a},0}}{\rho_c} g \sin\beta - \frac{1}{2}\frac{\rho_{\text{a},0}}{\rho_c} \text{C}_c u_c^2, \tag{41}$$

which is mathematically similar to the block model described in De Blasio (2011), where $\rho_c = (1 - e)\rho + e\rho_{a,\ 0}$ is the density of the cloud, u_c its velocity, e is the ratio between the volume of the ambient air and the total volume of cloud, C_c is the equivalent drag coefficient between the cloud and both ambient air and the ground (Bridge & Demicco, 2008), and β is the slope angle. The problem of cloud propagation belongs to the general class of dust cloud flows, and thus, it has already been considered in the study of turbidity currents (e.g., Bridge & Demicco, 2008), pyroclastic flows (Branney & Kokelaar, 1997), and powder snow avalanches (Fukushima & Parker, 1990). To our knowledge, no previous work has quantitatively addressed the problem of dust clouds composed of fragmented rock.

The equivalent drag coefficient is a function of the front drag, skin friction, and basal friction coefficients as well as of the cloud size. Its mathematical expression is similar to the one adopted for rock avalanches traveling in water (De Blasio, 2011)

$$C_c = \frac{C_{cf}}{l_c} + 2\frac{C_{cs}}{w_c} + \frac{C_{cf}}{h_c} + \frac{C_{cb}}{h_c}, \tag{42}$$

where C_{cf} is the front drag coefficient, C_{cs} is the skin friction coefficient, and C_{cb} is the basal friction. Grains of the cloud are maintained aloft by the turbulence developed within the current (Bridge & Demicco, 2008) as well as by the long settling time of the grains. After an initial stage the cloud velocity reaches asymptotically a limit (u_c^{lim}), which corresponds to the equilibrium condition between the drag force and gravity

$$u_c^{lim} = \sqrt{\frac{2}{C_c}\frac{\rho_c - \rho_{a,0}}{\rho_{a,0}} g \sin\beta}. \tag{43}$$

The degree of dilution represents the ratio between the cloud volume and the initial volume of the part of the block that constitutes the cloud.

4.5. Cloud Settling

It has been observed that several minutes to hours after an EER, the resulting dust cloud comes to a halt and finally begins to settle. For example, during the Gran Sasso EER in Italy, the A24 motorway had to be temporarily closed (Bianchi-Fasani et al., 2013, 2008). We calculate the settling time for a hypothetical height of 100 m of still air composed of powder-sized grains as a function of their diameter calculated with the drag coefficients recommended by Rhodes (1998). Our computation of the settling time was performed by considering the motion of a single small clast of sphericity index ψ subject to both gravity force and air drag force, which depends on the particle Reynolds number (Rhodes, 1998). A particle will initially accelerate until the corresponding limit velocity is reached, corresponding to the equilibrium between gravity and drag force, after which it travels at constant velocity. Thus, the deposition is computed by considering the limit velocity. It follows that for particles of diameter smaller than 0.01 cm, the falling time may increase dramatically to several minutes, hours, or even days for particles on the order of 10 microns (Figure 6b).

4.6. An Empirical Rule for Damage Area

As described above, the devastation caused by an EER extends much beyond the point of impact. For practical purposes of risk estimate, it is useful to establish a semiempirical law for the damaged area. Carpinteri and Pugno (2002) proposed an empirical relationship for transient explosive phenomena from different energy sources including nuclear explosions and meteoroid impacts. According to Carpinteri and Pugno (2002), the damaged area A_D as a function of the energy E_{kf} released in the explosion is

$$A_D\left(\mathrm{km}^2\right) \approx K\left[E_{kf}\left(\mathrm{TJ}\right)\right]^{0.67}, \tag{44}$$

where E_{kf} is expressed in TJ and A_D in km^2. Carpinteri and Pugno (2002) find a good correlation with nuclear explosions using K = 1.5 km^2 TJ$^{-0.67}$. Note that the exponent close to 2/3 probably indicates a volume-to-surface effect. In applying the above equation to the EERs, the kinetic energy of fragments E_{kf} should be used rather than the potential energy.

5. Case Studies

In this section, the models previously introduced are applied to reproduce the processes occurring during an EER. Since the data required to calibrate the model are not usually collected in rockfall inventories, we chose three case studies that provide a reasonable combination of data availability and event recording (photos, movies, and seismic records), differences in lithology and affected volume, and where it was possible for us to collect additional field data for the model. The three case studies are the Happy Isles 1996, the Cengalo 2016, and the Cima Una 2007 EERs. For each case study, a brief description of the event is given, providing the grain size data, parameter calibration and estimates of the different forms of energies, analysis of

the dust cloud, and finally of the damage area (which was accomplished by modifying Carpinteri & Pugno, 2002).

5.1. Happy Isles

5.1.1. Brief Description

The Happy Isles rockfall in Yosemite National Park (California) was the first well documented case of EER (Wieczorek, 2002; Wieczorek et al., 2000, 2008). It occurred on 10 July 1996 (6:52 p.m.), and it is one of a series of rockfalls that have occurred in Yosemite Valley (Stock et al., 2011; Stock et al., 2013; Wieczorek, 2002; Zimmer et al., 2012). Two large rockfalls (23,000 and 38,000 m^3) detached along exfoliation joints in granodioritic and tonalitic rocks (Sentinel granodiorite), descended vertically over 150 m along a steep slope before jumping from a natural ramp for an additional fall of 550 m (Wieczorek, 2002; Wieczorek et al., 2000). The blocks hit the talus in sequence at a calculated velocity of about 120 m/s (Wieczorek et al., 2000) leaving small mounds of debris. The event produced a magnitude *M* 2.15 seismic wave, with seismic records showing two impacts 13.6 s apart (Wieczorek, 2002). Atmospheric pressure waves were generated, with a probable frontal weak shock wave, and strong wind gusts and airblast affected the downslope area. Wieczorek et al. (2000) estimated that the airblast reached the speed of sound within the dusty atmosphere (120–130 m/s). Trees were abruptly uprooted and snapped by the airblast within an area of ~0.13 km^2 up to about 540 m from the main impact point. The trees were laying downslope and oriented radially from the impact point. The impact generated a dense dust cloud of pulverized rock, which propagated downslope, stripping bark from downed trees, and snapping branches from tree trunks (estimated wind speed of 84–95 m/s, Wieczorek et al., 2000) and leaving a sandy to gravelly cover along the talus. Small rock fragments pierced the tree trunks and were found at distances up to about 200 m from the impact. At distances longer than 350 m from the impact only some tree tops were snapped off (wind speed ~40 m/s).

5.1.2. Analysis

Figure 7 shows the comparison between some selected granulometric curves by Wieczorek et al. (2008) and the corresponding fitting obtained by the homographic, Weibull, NGEV (Normalized Generalized Extreme Value distribution), and lognormal distributions (equations (18), (21), (22), and (24), respectively). Table S1 (supporting information) shows the corresponding value of the minimized target function indicated as error. The best fit is attained by the homographic curve and this has been used for the successive computations. The initial value of the block volume (supporting information Table S2) equaled the minimum value of the total destabilized block mass reported in Wieczorek et al. (2008).

Using equation (14), the areal extent of fragmented debris was estimated according to the four grain size curves (supporting information Table S2). Differences in the estimated areal extent of fragmented debris are due to the differences of the granulometric curves obtained for samples collected at different sampling points. Coupling equations (2), (4), (5), and (11) allows calculation of the various energy contributions involved in the impact and fragmentation process. The results obtained are summarized in Table S3 (supporting information), where the fragmentation efficiency and the disintegration number are also considered. In the above calculations, the parameters of the fragmentation specific energy function $\gamma(D)$ are $\gamma_0 = 2.67\ J/m^2$, $\alpha = 0.60$ and $D_0 = 1 \cdot 10^{-8}$ m (see Tromans & Meech, 2004, for the α quartz).

To determine the fragmentation energy, we first need to estimate the fraction of the boulder mass transformed into the sandy-powdery fraction (section 5.1). Data gathered by Wieczorek et al. (2007) show that the largest blocks were deposited on a steep and volumetrically significant talus, while the powdery fraction, whose volume we need to evaluate, was deposited beyond this talus. To calculate the fraction η_v, we thus interpolated the isopach curves presented by Wieczorek (2002) and Wieczorek et al. (2007) and found a volume of the sandy-powdery fraction $\eta_v V_b = 1{,}437 m^3$ corresponding to a value $\eta_v = 0.062$.

The fragmentation energy does not reach large values compared to the initial potential energy of the block ($\frac{E_f}{E_0} < 0.3\%$, see also Table S3). As a consequence, the energy acquired by the fragments is a large fraction (~99.2%) of the initial potential energy. Note that the seismic energy, being on the order of $10^{-5} - 10^{-6}\ E_0$, is completely negligible in comparison with the fragmentation energy (Table 3). The other forms of energy loss such as air drag (section 3.3.1), seismic waves (section 3.3.2), sound (section 3.3.3), and plastic deformation (section 3.3.5) are also negligible according to the previous analysis. This could explain the extreme abrasive effects shown on the foliage and trees described by Wieczorek et al. (2008). Equations (36)–(40) are used in the shock wave calculations for radial distances of 100, 400, and 1,000 m

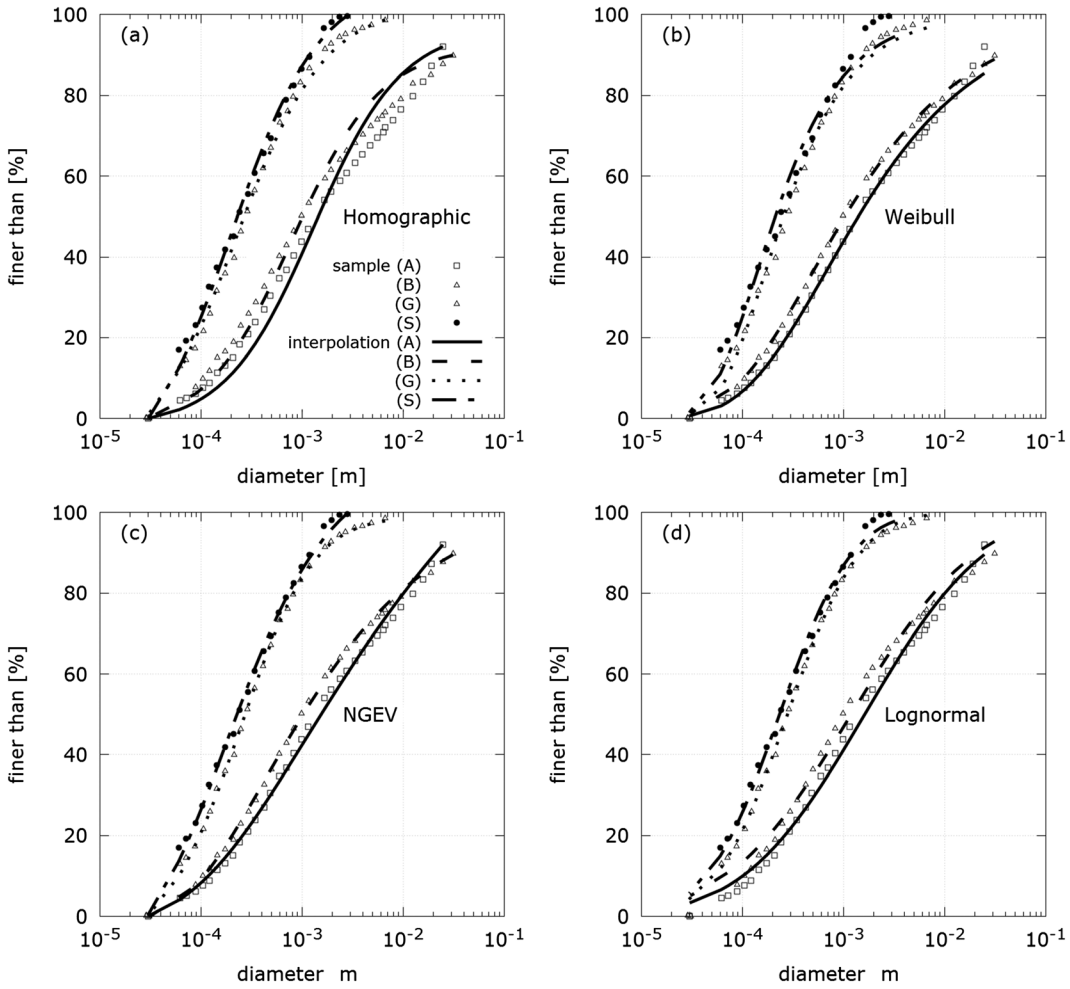

Figure 7. Comparison between the experimental grain size curves and the fitting curves for the Happy Isles study case. Data from Wieczorek et al. (2000): (a) the homographic curve (equation (18)); (b) the Weibull curve (equation (21)); (c) the normalized generalized extreme value, NGEV, (equation (22)): (d) the lognormal curve (equation (24)).

from the impact point (Table 4). The results for the overpressure are close (within 2.3%) to the ones reported by Morrissey et al. (1999).

5.2. Cengalo

5.2.1. Brief Description

The Pizzo Cengalo, a major granodioritic rock peak of the Central Alps, has been affected in the last decade by a series of major rockfall events on the Swiss side. Some large rockfalls were initially observed in 2003 and documented in 2009. The sequence of major events started on 19 July 2011 (6.00 a.m.) followed by frequent rockfalls. On 27 December 2011 (17:25 UTC) a $1.5 \cdot 10^6$ m^3 rockfall occurred from the upper portion (~3,200 m above sea level, asl) of the NE wall of the Cengalo. The event was recorded by the Swiss and the German seismic networks with an equivalent magnitude $M = 2.7$ and a total duration of about 2 min. The rockfall mass was subdivided by the local topography during the initial fall, with most of it directed along the NNW sectors. The material reached the valley down to about 1,440 m asl and a very large dust cloud affected the valley. A few years later, on September 2016 a series of rockfalls occurred before another 150,000 m^3 rockfall on 11 September (hypertext 2 and 3 in supporting information). Again, the mass spread over a large portion of the talus, developing a large dust cloud.

More recently, increasing rockfall activity has been observed starting from 24 June 2017, with larger rockfalls since 13 August, and a major event on 21 August (11:29 a.m.) that was slightly smaller than the one in 2016

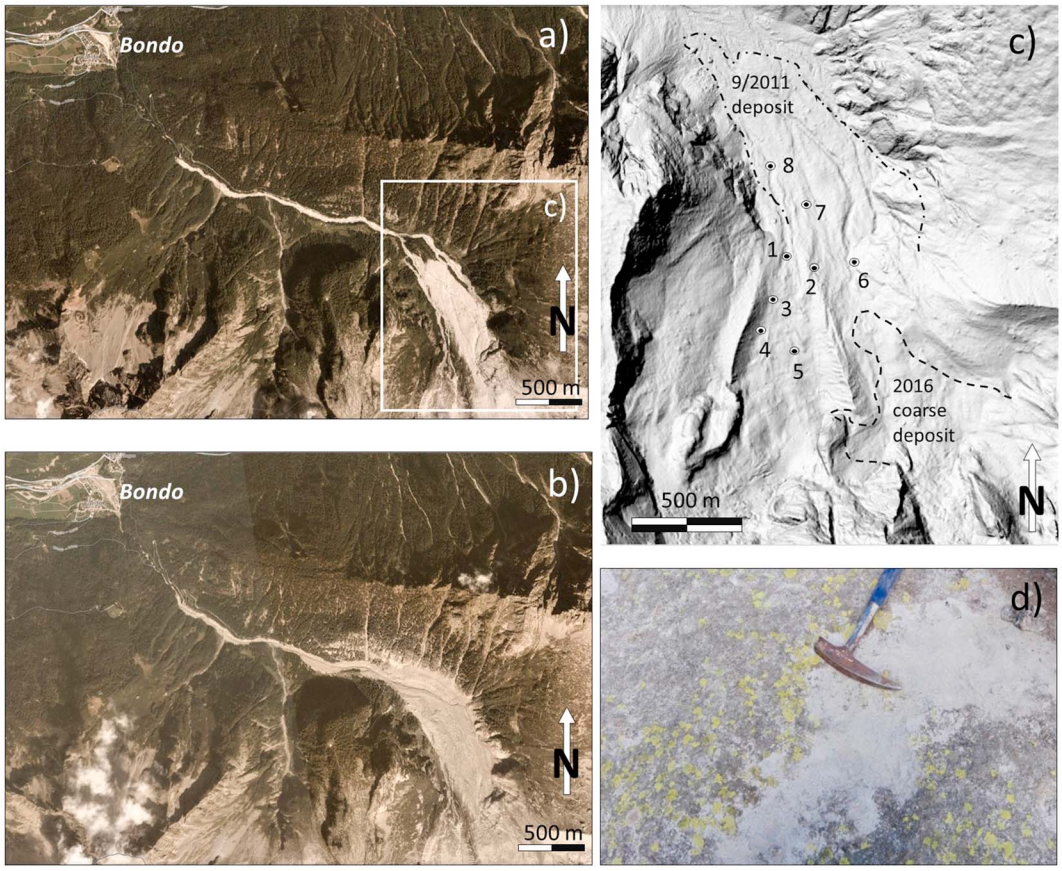

Figure 8. The Cengalo extremely energetic rockfall deposits: (a) deposit of the September 2011 Cengalo event and position of the area represented in Figure 8c; (b) extent of the deposits of August 2017 event (Planet Team, 2017) and of the debris flow phenomena affecting the middle portion of the valley and the alluvial fan (Bondo); (c) limits of the 2011 and 2016 coarse deposition areas and position of the sampling points with their identification number. Sampling of the 2016 extremely energetic rockfall dust cloud deposits covered the portions beyond the coarse deposit limit; and (d) typical appearance of the powder deposit at the sampling points.

(recorded seismic magnitude: $M = 2.3$). On 23 August 2017 (9:30 a.m.), $4 \cdot 10^6$ m^3 of rock and debris (recorded magnitude $M = 3$; hypertext 6 and 7 of supporting information) detached from the cliff (at about 3,000 m asl), engulfing the entire slope down to about 1,350 m asl. This was followed by another secondary large rockfall (11:36 a.m., $M = 2.1$). Seismic energy was thus on the order of 10^{-4}–10^{-6} of the initial block potential energy (see Table 3).

After the rockfall, a large debris flow reached the main valley, filling a preexisting sedimentation basin and partially damming the Mera River (hypertext 8 and 9 of supporting information). On the following days (25 and 29 August) more debris flows reached the alluvial fan on which the Bondo village is located (hypertext 9 of supporting information). The EER event caused eight casualties. The 23 August 2017 event involved about 3.5 Mm^3 of material of which 0.5 Mm^3 are attributed to the contribution of ice eroded from the small glacier at the toe of the cliff. A similar but slightly larger volume is estimated for the deposit.

5.2.2. Clast Size Distribution and Fragmentation Energy

During the summer of 2016, immediately after the event, samples from eight different locations were collected downslope from the impact point and taken to the laboratory for granulometric analysis with a laser granulometer (Hydro2000MU-Mastersizer). Figures 9a and 9b shows a comparison between the experimental data and those obtained by the homographic and Weibull interpolations, respectively. In this case, we find that the best fit was provided by the normalized GEV distribution, with values of the parameters ξ, μ,and σ reported in Table S4 (supporting information).

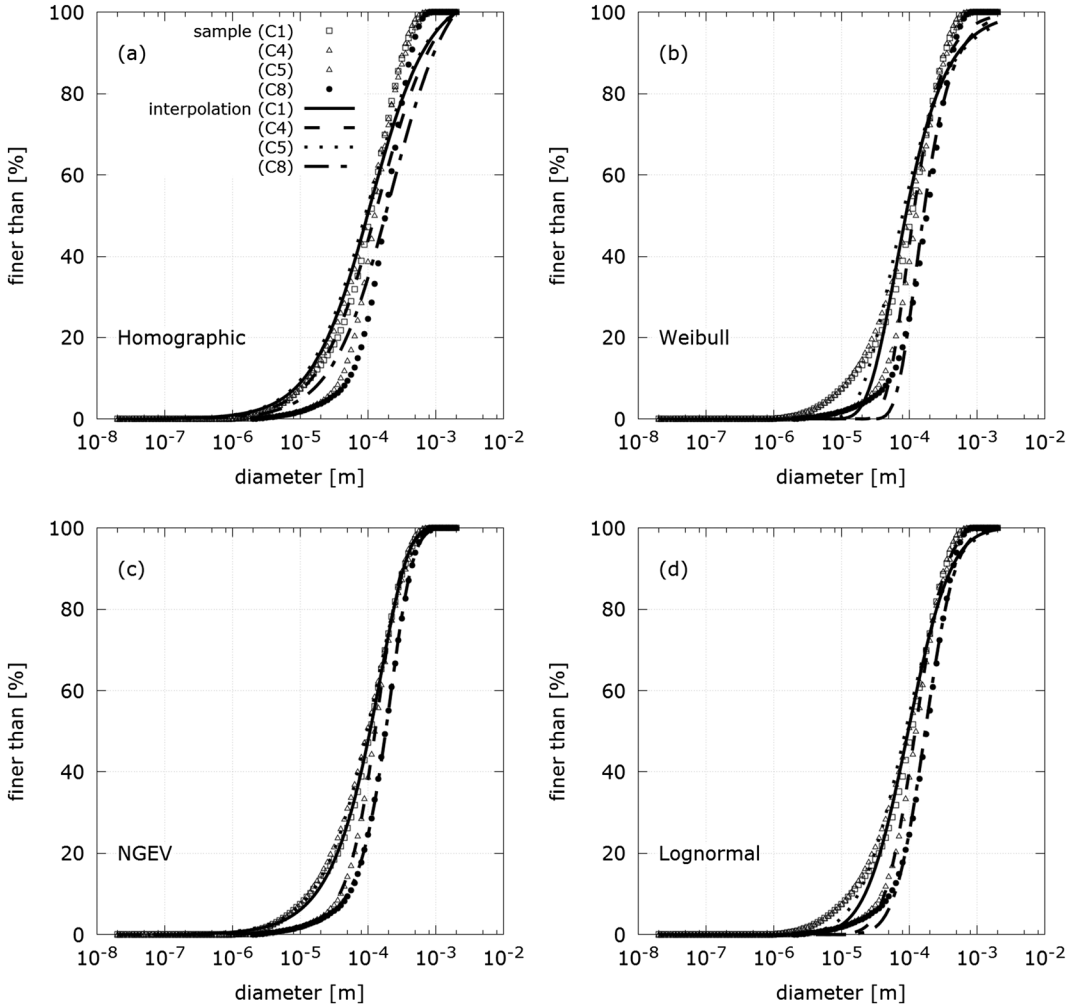

Figure 9. Comparison between the experimental grain size curves and the fitting curves for the Cengalo study case. Data from our sampling: (a) the homographic curve (equation (18)); (b) the Weibull curve (equation (21)); (c) the normalized generalized extreme value, NGEV, (equation (22)): (d) the lognormal curve (equation (24)).

The areal extent of the fragmentation deposit obtained from the computation (supporting information Table S5) changes according to the chosen sample. This seems related to the position of the samples and in particular with the distance from the impact source. The C_8 sample (see Figure 8 for position) is characterized by larger clasts compared to the others, which is likely a consequence of the more efficient transport of smaller particles in the dust cloud. Although the distributions are not extremely different from each other, the resulting areal extent of fragmented material may differ by a factor 2 (cf. sample C_1 with sample C_8). This is because the areal extent of fragmented material is sensitive to the population of small particles. However, in this case as for the Happy Isles event, part of the rockfall was deposited directly in the form of relatively large blocks. Considering the initial size of the failure (ca. $V = 150,000\ m^3$) and the average thickness of the deposit of large blocks on the slope (0.5 m), the volume of rock that possibly underwent intense fragmentation can be estimated at about 67,500 m^3 ($\eta_v = 0.45$). The fragmentation energy at Cengalo is typically 18% of the initial block potential energy, but is as high as 78–92% for the C1 and C5 events, respectively.

The energy computations are illustrated in Table S6 (supporting information), using the parameters of the fragmentation specific energy function $\gamma(D)$ equal to $\gamma_0 = 2.67\ J/m^2$, $\alpha = 0.60$, and $D_0 = 1 \cdot 10^{-8}$ m.

5.2.3. Cloud Propagation

For the 2016 Cengalo EER (Figure 8b), several videos allow us to reconstruct the behavior of the dust cloud formed immediately after the main impact. From the videos (see list in supporting information), we

extracted an initial velocity value of about 20 m/s for the cloud traveling downslope. The videos show that the cloud thickness does not change dramatically in time at the beginning of the motion, while it increases toward the end due to particle dispersion in the air. A progressive decrease in velocity from about 20 (72 km/hr) to 8 m/s (28.8 km/he) was computed from the videos, and it is similar to values extracted for the 21 August 2017 event. To calculate the cloud velocity in our model, we use equation (43) in which we use the cloud size estimated from the videos. Sizes change due to lateral and vertical spread as well as horizontal stretching. We compare the calculated and measured cloud velocities at two instants: (i) when the cloud reaches a relatively gentle slope of 22° and (ii) when the cloud, after traveling 300 m along the same slope, disappears from the frame. During the motion, it is assumed that the total mass of the suspended particles is constant and equal to 100,000 kg, and thus, the cloud density depends only on its size. This estimate neglects settling of the cloud during motion and the opposite process of entrainment. At the first instant of time (w_c = 100 m, l_c = 100 m and h_c = 50 m), the cloud has a volume of 500,000 m^3 and its density is 1.34 kg/m^3, whereas at the second instant of time the cloud spreads (w_c = 300 m, l_c = 400 m and h_c = 200 m) and its volume is 24,000,000 m^3, with a density of 1.14 kg/m^3.

The drag coefficients C_{cf}, C_{cs}, and C_{cb} play an important role in the velocity computation. To our knowledge, these coefficients are unknown for this kind of dust clouds. Some insight can be gained based on phenomena, which are dynamically similar, such as powder snow avalanches (Sovilla et al., 2008), pyroclastic flows (Doyle et al., 2008), and turbidity currents (Bridge & Demicco, 2008). Calculated velocities for the two temporal instants are reported in Table S5 (supporting information) based on the parameters of Table S4 (supporting information).

According to equation (43), during the cloud motion two opposite effects control the cloud velocity: the variation of cloud density ρ_c and the drag coefficient C_c, which in turn depends on the cloud size. It turns out that density is the dominant factor, which explains the velocity decrease from 16.5 (59.4 km/hr) to 5.14 m/s (18.5 km/hr) during the flow. The comparison between the final values obtained from videos (8 m/s or equivalently 28.8 km/hr) and the corresponding model predictions (5.14 m/s or 18.5 km/hr) is satisfactory, even though more in situ data are required for a complete validation.

We also examined the peculiar cloud formed during the August 2017 event (Figure 10). After the initial collapse, a very fast whitish cloud traveled beyond the rest of the darker rock cloud body at 18 s, as reported in Figure 10. We estimate from the video 8 (supporting information) an astonishing velocity for such a cloud of 100 m/s from the moment it becomes evident in the movie. We suggest that this velocity was inherited from the rock block collapsing directly onto the flank at an estimated velocity of 100 m/s. After the initial impact with the mountain flank, the cloud direction changed by 90° as a consequence of the local valley topography. Thus, the cloud velocity does not correspond to the limit velocity equation (43).

5.3. Cima Una

5.3.1. Brief Description

On 12 October 2007 (8:40 a.m.) a 40,000 m^3 rockfall occurred in the upper Fiscalina Valley (Sesto Dolomites, Bolzano, and Northeastern Italian Alps) at Cima Una (2,698 m asl). The main collapse was followed by a series of small rock falls. The collapse affected the very top of the mountain peak (between 2,690 and 2,610 m asl) and the dolostone rock mass fell for about 900 m along the subvertical cliff, with some secondary impacts against ledges, and reached the 30°–35° talus slope. The event was recorded by the Austrian and Italian seismic stations (20 to 80 km away), and a local magnitude of about M = 0.8 was assigned. Seismic energy was thus on the order of 10^{-8} of the initial block potential energy (see Table 3).

The rock fragments reached a maximum distance of 800 m from the cliff toe. A dense dust cloud traveled about 4 km along the valley bottom, depositing over about 2.7 km^2 with a thickness ranging from 1 up to 100 mm (on the upslope side of larger blocks), and progressively decreasing with distance. Local winds transported the finer dust over a total 13 km^2 area. According to Viero et al. (2013), the deposit was mainly composed of fine material up to a volume of $32 \pm 4 \cdot 10^3$ m^3 with relatively few boulders. The boulders reached a maximum distance of about 550 m from the toe of the rock wall, leaving impact craters up to 40-cm deep. Ninety-nine blocks (generally smaller than 2 m^3, maximum volume 7 m^3) were mapped by Viero et al. (2013) for a total volume ranging between 50 and 90 m^3. An average of 17 cm (±3 cm) of fine debris was deposited above the talus slope, covering a total $64 \cdot 10^3$ m^2 and resulting in an approximate volume of

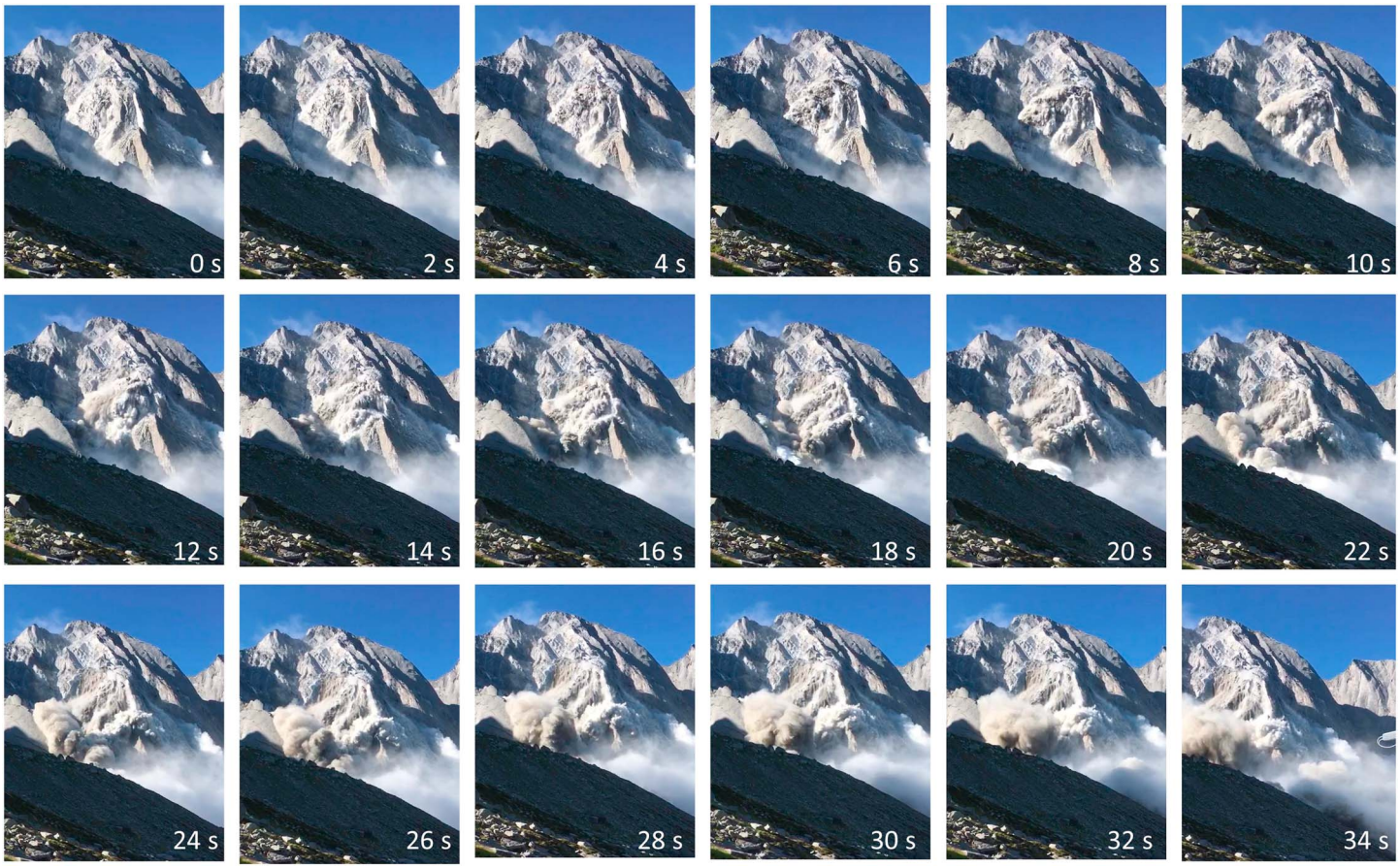

Figure 10. Sequence of the August 2017 Cengalo event. Starting from frame at 18 s and for a duration of about 4 s, an extremely fast white cloud travels downward toward the right. The estimated cloud front velocity is 100 m/s. This does not correspond to the steady state propagation velocity of the cloud along the open slope (*from video by R. and B. Salis*).

11(±2) 10^3 m^3. The associated air blast broke and uprooted trees over a 50,000 m^2 area, snapping branches and locally peeling the bark off some of the trunks.

5.3.2. Clast Size Distribution and Fragmentation Energy

The granulometric spectra for the case of the Cima Una EER in the Italian Alps (Table 1 and Figure 2) have been reported in the literature (Viero et al., 2013) and confirmed by our samples on which grainsize and SEM analyses (Figure 4) were performed. These allow us to calculate the fragmentation energy. Table S9 (supporting information) shows the parameters employed to fit the granulometric curve, and Figure 9 illustrates the comparison between the experimental data and the best fitting curves. Table S10 (supporting information) shows the computation of the areal extent of fragmentation determined from Weibull distribution, and Table S7 (supporting information) reports the energies involved. The results of the energy computations, using the same parameters γ_0, α, and D_0 adopted for the previous case studies, are reported in Table S11. The fragmentation energy at Cima Una ranges from 1–18% of the initial potential energy of the block.

5.4. Damage Area Estimates

Using the data for the cases of the Happy Isles and Cima Una events (damage area of 0.1–0.2 and 0.05 km^2, respectively), we found a good correlation for equation (44) with $K = 0.28$ km^2 $TJ^{-0.67}$ such that the modified semiempirical relationship is

$$A_D\left(\mathrm{km}^2\right) \approx 0.28\ [E_{kf}(\mathrm{TJ})]^{0.67}. \tag{45}$$

For the 2016 Cengalo EER, this formula (45) estimates an area of 0.34 km^2, but the absence of vegetation does not allow a direct comparison with this result.

We have used a similar formula to fit the areal distribution of the dust cloud as a function of the energy released for which more complete data are available. Starting from photos and videos of the events listed in Table 1, we estimate the area covered by the denser part of dust cloud for each event. In order to evaluate the robustness of this approach, the bootstrapping approach has been adopted to distinguish our predictions from a simple fit to the data. The bootstrapping procedure (Efron & Tibshirani, 1994) consists in replicated fitting of subsets of randomly resampled data pairs, and consequent computation of mean and standard deviation for the two power law coefficients. The resulting cloud of data points for the values of the coefficient K and the exponent are further discussed in Figure S1 of the supporting information. Our relation for the area covered by dust is so

$$A_{\mathrm{Dust}}\left(\mathrm{km}^2\right) \approx 0.345\ \left[E_{kf}(\mathrm{TJ})\right]^{0.547}. \tag{46}$$

6. Discussion

Our calculations for the case studies show that the fragmentation is a relatively small fraction (0.2%–18.2%) of the initial block potential energy (except for the Cengalo C_1 and C_5 events, 77.6% and 92.2%, respectively), while the other forms of energy loss (air drag, seismic, sound, and plastic deformation) are expected to be negligible (sections 3.3.1–3.3.5). Thus, a large percentage of the initial block potential energy (more than 80%) is promptly converted into kinetic energy of the fragments (ballistic projection, shock wave, sand blasting, and dust could propagation). Calculated fragment velocities on the order of a few hundred meters per second may explain the devastation observed beyond the impact point.

The experimental grain size curves illustrated in Figures 7, 9, and 11 show that the ranges of particle diameters produced during an EER are very wide. Field evidence reveals that during the sudden fragmentation process, part of the original block produces some large fragments (gravel- to boulder-sized clasts), whereas the rest of the block is converted to powder. This implies that the granulometric curve of all fragments is bimodal, in which the two peaks correspond to dust and large clasts, respectively. Since the energy needed for fragmentation increases with decreasing dust size, most of the fragmentation energy is spent in producing dust, rather than larger clasts and, for this reason, the contribution of the large clasts to the fragmentation energy has been neglected (see discussion at the end of section 3.4.1).

Another important feature related to the energy budget and the computation of fragmentation energy is the dependence between the powder spectrum and the distance between the source area and the impact point. We find that at greater distances from the impact point, the particle diameters are reduced (grain size curves become steeper, more uniform, and shifted toward the smaller diameters). Our samples and those published by Viero et al. (2013) for the Cima Una EER show such gradation and sorting with distance. Our explanation is that since the smaller particles are more mobile and have longer settling times, they are able to travel longer distances within the dust cloud than larger particles.

There is much work that needs to be done to better understand the dynamics of EERs. First, the fragmentation energy as a function of the clast size needs to be better understood. As discussed above, the fragmentation specific energy increases rapidly with decreasing clast size, which likely influences the energy budget. In addition, Grady and Kipp (1987) observed a direct strength dependence on the strain rate. This can have a major influence on the required fragmentation energy for very large drop heights when the impact velocity is extremely high. The same effect has been observed in numerical discrete element simulations of coal fragmentation by Zhao et al. (2017), which show that during fragmentation, a decrease of fragment size is associated with an increase in fracture stress and strain rate. These nonlinear, time-dependent controls of particle size and fragmentation energy will determine the amount of material that is generated by fragmentation in each grain size class. However, even a complete theory of fragmentation may be hampered by a lack of knowledge regarding the fraction of large-size fragments with respect to the total amount of initial EER mass. Unfortunately, this type of data is scarce, and even the size of the block (or blocks) at the impact is usually quite variable and obscure, allowing only for a rough estimate of the energy budget. Therefore, this data should be collected for future events if a more exact estimate of the EER dynamics, hazard, and risk, is required. At a minimum, as a useful starting point, the percentage of large clasts should be measured with care, allowing volumetric differentiation of the finely fragmented mass.

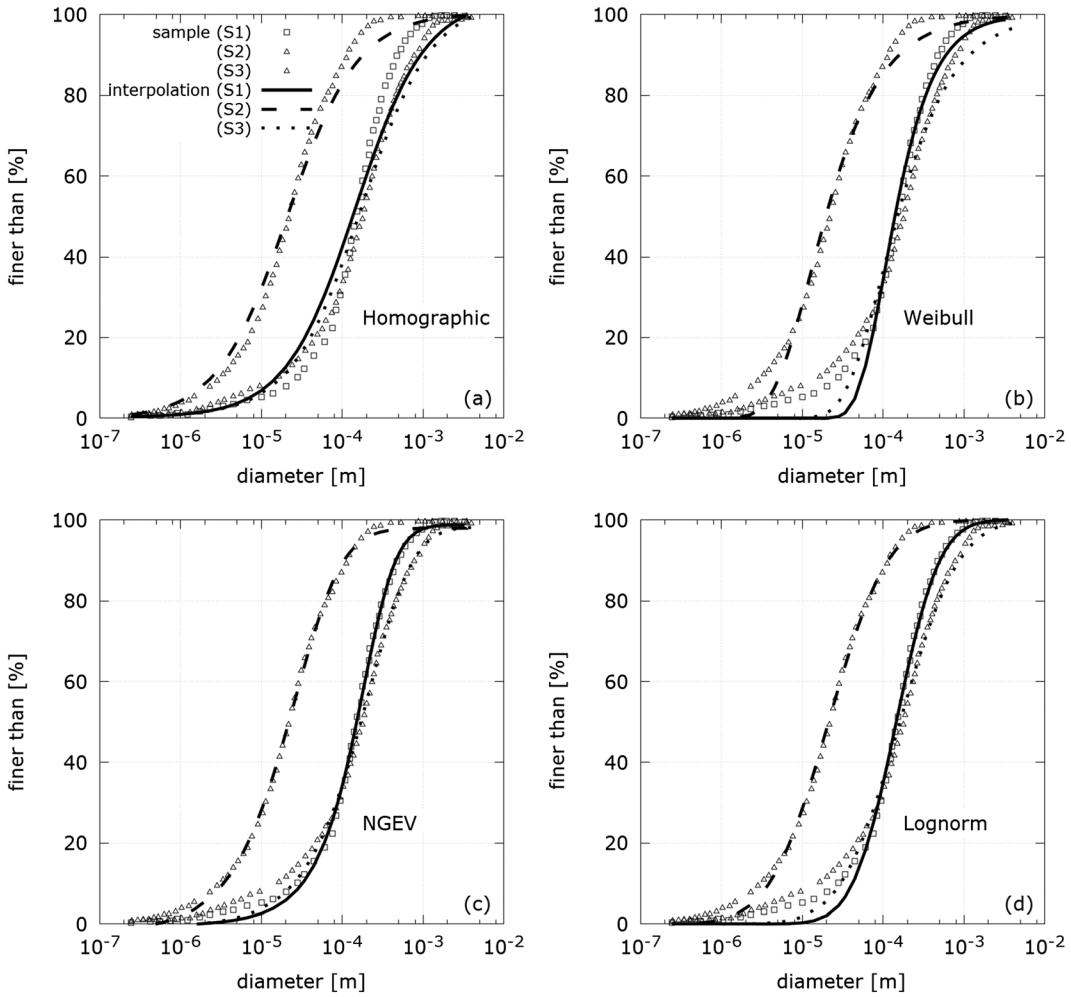

Figure 11. Comparison between the experimental grain size curves and the fitting curves for Cima Una case study. Data from Viero et al. (2013): (a) the homographic curve (equation (18)); (b) the Weibull curve (equation (21)); (c) the normalized generalized extreme value, NGEV, (equation (22)): (d) the lognormal curve (equation (24)).

Another issue concerns the best expression for the smallest clasts. In the presented case studies, two different expressions are found to fit well the fragment distribution: the homographic curve for the Happy Isles EER, and the Weibull distribution for the Cengalo and Cima Una EERs. This difference can be perhaps attributed to a variety of causes, such as different lithologies involved (microcrystalline granite in the case of Happy Isles and Cengalo EERs, and the dolostone of Cima Una EER) and to the relative position of the samples with respect to the slope geometry and the deposit. It is therefore difficult to disentangle the various contributions by sampling deposits at different points in cases where EER events have extremely variable characteristics. Future investigations should also account for the kinetics of fragmentation. For example, De Blasio and Crosta (2014) investigated a bin model for rock avalanches to produce a clast size spectrum, which can be in principle compared to the measured ones.

Concerning hazard and risk zonation, it is important to study the semiempirical relationships starting from the ones suggested by Glasstone and Dolan (1977) and by Carpinteri and Pugno (2002) for explosions. In general, these equations predict that increasing fragmentation, or consuming more energy for the fragmentation, leaves less energy for the subsequent ballistic and blasting evolution. This results in a more limited extent of the damage area, which scales with a 2/3 exponent, suggesting a possible surface-to-volume effect. The relationship proposed here has a lower coefficient (0.28) with respect to the one (1.5) proposed by Carpinteri and Pugno (2002). This difference could suggest smaller efficiency of natural fragmentation mechanisms compared to those associated with

a nuclear explosion, but more case studies should be reported to better constrain the values of the constants.

6.1. Model Uncertainty

As mentioned above, the proposed model includes a large number of variables, some of them difficult to fully constrain without detailed in situ studies or material characterization. At the same time, some local environmental conditions could control the amount of fragmentation and of generated dust. As a consequence, some considerations can be drawn to support the use of the model and to report some sources of uncertainty. In the following some of these problems are introduced and discussed.

The study of fragmentation is performed experimentally and provides values of the fragmentation specific energy. Unfortunately, the specific fragmentation energy depends on many variables including temperature, water content, grain or crystal size, and sample size. As a consequence, mean values are normally reported. Experimental data demonstrate that the energy required for fracture and comminution increases with decreasing particle size (Bieniawski, 1977; McDowell & Bolton, 1998; Weiss et al., 2014). Therefore, we proposed a power law relationship to take into account this phenomenon. However, the value of the coefficient α (equation (17)) cannot be directly calibrated due to the lack of experimental data. Therefore, the present work cannot claim to match the exact values of in situ observations. Rather, it proposes a methodology that in principle allows obtaining the fragmentation energy starting from the granulometric curve and taking into account the increment of specific fragmentation energy with decreasing clast size. Nevertheless, even if more experimental data were available, the model would still be affected by some uncertainty associated with the variability of specific energy and by other site specific characteristics (e.g., block lithology, crystal or grain size, initial degree of subdivision of the rock mass, degree of saturation, occurrence of multiple impacts, and impacts on rockfall ledges).

Another source of inaccuracy lays in the bias introduced by the mapping and sampling procedure of very thin and dispersed dust deposits. Indeed, the dust cloud movement generates a heterogeneous settling process due to different deposition times of particles with different size. Therefore, the grain size curve for a specific sample or representative of an event depends on the sampling location and on the distribution and quantity of sampling points (Figures 7 and 11). In turn, the granulometric curve affects significantly the generated surface and thus, the fragmentation energy values, especially for strongly changing values of the minimum particle diameter. This uncertainty could be partially solved or reduced by considering the effect of sample position on grain size curve characteristics or by carrying out systematic sampling and testing campaigns.

The evaluation of the percentage of the initial volume converted into the dust cloud can generate further uncertainty. This percentage is worked out as the difference between the initial block volume and the total volume of the large clasts and boulders in the deposit. Both the estimate of the initial block volume and the total volume associated with the large clasts do not give large errors except for events occurring in remote areas where no previous topographic data or observations are available. Even if it is not always possible to detect all the large clasts and their volume, this uncertainty seems limited or more easily constrained by in situ observations. The description of the impact crater geometry can introduce some inaccuracy in the energy budget, but considering its weight in the computation, this is believed to be small.

Moreover, at some of the study sites, access to the area was difficult or forbidden by local authorities for safety reasons, making it impossible to carry out a complete survey immediately after the events. This can cause errors especially in the mapping of the dust cloud deposits that are ephemeral in nature.

We also note that the movement of the dust cloud is assumed to occur freely without obstacles that could influence its trajectory. This condition is not always satisfied because infrastructure and natural barriers can influence significantly the cloud motion inducing anomalous deposition. An example is reported in Figure 10 where the dust cloud front abruptly changes direction and velocity due to the presence of a sharp topographic obstacle. In addition to the change in trajectory, the obstacle could generate a variation of the boundary layer modifying the flux regime, and consequently the motion and the area affected by the dust cloud.

Finally, better data for many more events will likely reduce the present uncertainty for the mathematical relationship between the energy released and the damaged area derived in this study (equation (45)).

7. Summary

EERs are suggested here as a class of cliff fall phenomena. They can cause damage and losses by direct impact, ballistic trajectories of large blocks, air blasting, and fine particle scouring. Modeling the chain of events can inform hazard and risk assessment. The paper introduced three conditions defining an EER, based on the specific energy, the total energy involved, and the suddenness of the energy released. We defined the disintegration number as the ratio between the energy per unit mass involved in the EER and the energy necessary to split a block in two, and we classified rockfalls into three categories (common, intermediate, EERs) according to the energy released, the disintegration number and the smallest fragment size.

To describe the chain of phenomena occurring during an EER, analytical formulations are introduced. The initial kinetic energy of fragments produced during impact is estimated and used to evaluate the initial clast velocity after the impact. By analyzing granulometric curves of deposited fragments, it is possible to estimate the areal extent of fragmented particles in the impact zone. For this purpose, the homographic curve is introduced to fit the experimental data, allowing one to evaluate a closed-form expression for the areal extent of fragmented particles produced by an EER.

Other functions are also adopted (i.e., Weibull, normalized generalized extreme value, and normalized log-normal). However, these last three distributions require numerical integration to obtain the value of the areal extent of fragmentation that, in turn, allows one to estimate the fragmentation energy.

We evaluated the abrasive effects of the fragments, the shock wave produced by the impact, and the corresponding wind velocity following the shock wave. The values obtained are sufficiently high to justify the effects observed for real EERs. The last phenomenon analyzed is the motion and deposition of the dust cloud produced. The maximum cloud velocity is evaluated through the definition of the slope angle and drag coefficients. Finally, the deposition model gives information about the settlement time, which can vary widely according to the particle size and shape.

We applied our theoretical model to several EER case studies where quantitative information was available. The analysis shows that fragmentation energy is relatively small (typically 0.2%–18% of the potential energy of the block), while other energy-consuming processes (air drag, seismic, sound, and ground deformation) are expected to be negligible (sections 3.3.1–3.3.5), which together explains the high kinetic energy of fragments and the severe damage by EERs. The model confirms the extent of damaged area according to a power law relationship.

It is hoped that more complete data and rockfall inventories will become available in the future, via monitoring cliffs that have the potential for producing EERs and through more quantitative study of the EER events and deposits. We suggest that the EER deposits should be further examined in order to report the grain size spectrum for different zones beyond the impact point and the volume percentage for different grain size ranges. Moreover, recently the availability of portable cameras and remote sensing methods will undoubtedly increase the knowledge of such phenomena in the future. All this information and data could allow a more complete testing of the proposed model and its validation.

Acknowledgments

We thank Davide Fusetti for performing the sampling campaign at the Cengalo EER and Paolo Gentile for assistance with the SEM analyses. We are grateful to the reviewers for deep insights and valuable comments that considerably improved our manuscript. All data used in preparation of this work are provided in the manuscript, references, and supporting Information, which includes a spreadsheet for the grain size data collected at Cima Una, Cengalo, Croda Rossa, and Gran Sasso. The work was supported by CARIPLO 2016-0756 —@RockHoRiZon—Advanced Tools for Rockfall Hazard and Risk zonation at the Regional Scale and by Project MIUR-Dipartimenti di Eccellenza 2018–2022.

References

Andrews, E. W., & Kim, K.-S. (1998). Threshold conditions for dynamic fragmentation of ceramic particles. *Mechanics of Materials*, *29*, 161–180. doi.org/10.1016/S0167-6636(98)00014-3

Atkinson, B. K. (1987). *Fracture mechanics of rock*, *Geology Series* (p. 553). London: Elsevier, Academic Press.

Bianchi-Fasani, G., Esposito, C., Lenti, L., Martino, S., Pecci, M., & Scarascia-Mugnozza, G. (2013). Seismic analysis of the Gran Sasso catastrophic rockfall (Central Italy). In C. Margottini, et al. (Eds.), *Landslide Science and Practice* (Vol. 6, pp. 263–267). Verlag Berlin Heidelberg: Springer. https://doi.org/10.1007/978-3-642-31319-6_36

Bianchi-Fasani, G. B., Esposito, C., Mugnozza, G. S., Stedile, L., & Pecci, M. (2008). The 22 August, 2006, anomalous rock fall along the Gran Sasso NE wall (Central Apennines, Italy). In *Landslides and engineered slopes. From the past to the future, two volumes+ CD-ROM: Proceedings of the 10th International Symposium on Landslides and Engineered Slopes, 30 June–4 July 2008* (pp. 355–362). Xi'an, China: CRC Press.

Bieniawski, Z. T. (1977). A review of coal pillar strength formulas by WA Hustrulid. *Rock Mechanics and Rock Engineering*, *10*(1), 107–110. https://doi.org/10.1007/BF01261805

Bond, F. C. (1952). The third theory of comminution. *Transactions of the American Institute of Mining and Metallurgical Engineers*, *193*, 494–496.

Branney, M. J., & Kokelaar, P. (1997). Giant bed from a sustained catastrophic density current flowing over topography: Acatlan ignimbrite, Mexico. *Geology*, *25*(2), 115–118. https://doi.org/10.1130/0091-7613(1997)025<0115:GBFASC>2.3.CO;2

Bridge, J., & Demicco, R. (2008). *Earth surface processes, landforms and sediment deposits*. Cambridge: Cambridge University Press. https://doi.org/10.1017/CBO9780511805516

Camp, W., Martin, R., & Chapman, L. F. (1962). Pain threshold and discrimination of pain intensity during brief exposure to intense noise. *Science*, *135*(3506), 788–789. https://doi.org/10.1126/science.135.3506.788

Carpinteri, A., & Pugno, N. (2002). One, two, and three-dimensional universal laws for fragmentation due to impact and explosion. *Transactions ASME*, *69*(6), 854–856. https://doi.org/10.1115/1.1488937

Corominas, J., Mavrouli, O., & Ruiz-Carulla, R. (2017). Rockfall Occurrence and Fragmentation. In K. Sassa, M. Mikoš, & Y. Yin (Eds.), *Workshop on world landslide forum* (pp. 75–97). Cham: Springer.

Crosta, G. B., Agliardi, F., Frattini, P., & Lari, S. (2015). Key issues in rock fall modeling, hazard and risk assessment for rockfall protection. In *Engineering geology for society and territory* (Vol. 2, pp. 43–58). Cham: Springer.

Crosta, G. B., Chen, H., & Lee, C. F. (2004). Replay of the 1987 Val Pola landslide, Italian alps. *Geomorphology*, *60*(1-2), 127–146. https://doi.org/10.1016/j.geomorph.2003.07.015

Crosta, G. B., Frattini, P., & Fusi, N. (2007). Fragmentation in the Val Pola rock avalanche, Italian Alps. *Journal of Geophysical Research*, *112*, F01006. https://doi.org/10.1029/2005JF000455

Davies, T. R., & McSaveney, M. J. (1999). Runout of dry granular avalanches. *Canadian Geotechnical Journal*, *36*(2), 313–320. https://doi.org/10.1139/t98-108

De Blasio, F. V. (2005). A simple dynamical model of landslide fragmentation during flow. In K. Senneset, et al. (Eds.), *Landslides and avalanches*, (pp. 95–100). London: Taylor and Francis.

De Blasio, F. V. (2011). *Introduction to the physics of landslides*, (p. 408). Dordrecht: Springer. https://doi.org/10.1007/978-94-007-1122-8

De Blasio, F. V., & Crosta, G. B. (2014). Simple physical model for the fragmentation of rock avalanches. *Acta Mechanica*, *225*(1), 243–252. https://doi.org/10.1007/s00707-013-0942-y

De Blasio, F. V., & Crosta, G. B. (2016). Extremely Energetic Rockfalls: Some preliminary estimates. In *Landslides and Engineered Slopes. Experience, Theory and Practice* (pp. 759–764). Boca Raton. FL: CRC Press.

Deline, P. (2001). Recent Brenva rock avalanches (Valley of Aosta): New chapter in an old story? *Geografia Fisica e Dinamica Quaternaria*, 55–63.

Deparis, J., Jongmans, D., Cotton, F., Baillet, L., Thouvenot, F., & Hantz, D. (2008). Analysis of rock-fall and rock-fall avalanche seismograms in the French Alps. *Bulletin of the Seismological Society of America*, *98*(4), 1781–1796. https://doi.org/10.1785/0120070082

Doyle, E. E., Hogg, A. J., Mader, H. M., & Sparks, R. S. J. (2008). Modeling dense pyroclastic basal flows from collapsing columns. *Geophysical Research Letters*, *35*, L04305. https://doi.org/10.1029/2007GL032585

Efron, B., & Tibshirani, R. J. (1994). An introduction to the bootstrap. CRC press.

Erismann, T. H., & Abele, G. (2001). *Dynamics of rockslides and rockfalls* (p. 316). Berlin Heielberg New York: Springer-Verlag.

Farin, M., Mangeney, A., de Rosny, J., Toussaint, R., & Trinh, P. T. (2018). Link between the dynamics of granular flows and the generated seismic signal: Insights from laboratory experiments. *Journal of Geophysical Research: Earth Surface*, *123*, 1407–1429. https://doi.org/10.1029/2017JF004296

Farin, M., Mangeney, A., Toussaint, R., Rosny, J. D., Shapiro, N., Dewez, T., & et al. (2015). Characterization of rockfalls from seismic signal: Insights from laboratory experiments. *Journal of Geophysical Research: Solid Earth*, *120*, 7102–7137. https://doi.org/10.1002/2015JB012331

Favreau, P., Mangeney, A., Lucas, A., Crosta, G., & Bouchut, F. (2010). Numerical modeling of landquakes. *Geophysical Research Letters*, *37*, L15305. https://doi.org/10.1029/2010GL043512

Frattini, P., Crosta, G. B., & Agliardi, F. (2012). Rockfall characterization and modeling. In J. J. Clague & D. Stead (Eds.), *Landslides: types, mechanisms and modeling* (pp. 267–281). Cambridge: Cambridge Univ Press.

Fries, M. M. (2013). Empirical and theoretical investigations on rock fall induced fly-rocks (Doctoral dissertation, ETH). p. 132

Fukushima, Y., & Parker, G. (1990). Numerical simulation of powder-snow avalanches. *Journal of Glaciology*, *36*(123), 229–237. https://doi.org/10.1017/S0022143000009485

Giacomini, A., Buzzi, O., Renard, B., & Giani, G. P. (2009). Experimental studies on fragmentation of rock falls on impact with rock surfaces. *International Journal of Rock Mechanics and Mining Sciences*, *46*(4), 708–715. https://doi.org/10.1016/j.ijrmms.2008.09.007

Gili, J. A., Ruiz-Carulla, R., Matas, G., Corominas, J., Lantada, N., Núñez, M. A., et al. (2016). *Experimental study on rockfall fragmentation: In situ test design and firsts results*, International Symposium Landslides 2016 (ISL2016), Napoli (Italia), (Vol. 2, pp. 983–990). Balkema: CRC Press.

Glasstone, S., & Dolan, P. J. (1977). *Effects of nuclear weapons* (p. 653). Washington, DC: US Department of Defense and US Department of Energy.

Gorlach, I. A. (2011). High velocity thermal gun for surface preparation and treatment. *The South African Journal of Industrial Engineering*, *13*(1).

Grady, D. E., & Kipp, M. E. (1987). Dynamic rock fragmentation. In B. K. Atkison (Ed.), *Fracture mechanics of rock*, (Vol. 10, p. 429–476). Academic Press.

Gualtieri, L., & Ekström, G. (2016). Seismic reconstruction of the 2012 Palisades rockfall using the analytical solution to Lamb's problem. *Bulletin of the Seismological Society of America*, *107*(1), 63–71. https://doi.org/10.1785/0120160238

Gutenberg, B., & Richter, C. F. (1956). Earthquake magnitude, intensity, energy, and acceleration (second paper). *Bulletin of the Seismological Society of America*, *46*(2), 105–145.

Hibert, C., Mangeney, A., Grandjean, G., Baillard, C., Rivet, D., Shapiro, N. M., et al. (2014). Automated identification, location, and volume estimation of rockfalls at Piton de la Fournaise volcano. *Journal of Geophysical Research: Earth Surface*, *116*, 1082–1105. https://doi.org/10.1029/2011JF002038

Hibert, C., Mangeney, A., Grandjean, G., & Shapiro, N. M. (2011). Slope instabilities in Dolomieu crater, Réunion Island: From seismic signals to rockfall characteristics. *Journal of Geophysical Research*, *116*, F04032. https://doi.org/10.1029/2011JF002038

Hofmann, R., & Mölk, M. (2012). Bemessungsvorschlag für Steinschlagschutzdämme. *Geotechnik*, *35*(1), 22–33. https://doi.org/10.1002/gete.201100021

Hogan, J. D., Rogers, R. J., Spray, J. G., & Boonsue, S. (2012). Dynamic fragmentation of granite for impact energies of 6–28J. *Engineering Fracture Mechanics*, *79*, 103–125. https://doi.org/10.1016/j.engfracmech.2011.10.006

Hughes, W. F., & Brighton, J. A. (1967). *Fluid dynamics*, *Schaum's outline series in engineering* (p. 265). New York: McGraw-Hill Book Company.

Kanamori, H. (1977). The energy release in great earthquakes. *Journal of Geophysical Research*, *82*(20), 2981–2987. https://doi.org/10.1029/JB082i020p02981

Kick, F. (1885). Das Gesetz der proportionalen Widerstände und seine Anwendungen: Nebst Versuchen über das Verhalten verschiedener Materialien bei gleichen Formänderungen sowohl unter der Presse als dem Schlagwerk. *A. Felix*

King, R. P. (2001). *Modeling and simulation of mineral processing systems*, (p. 405). Boston: Butterworth Heinemann.

Lambert, S., Heymann, A., Gotteland, P., & Nicot, F. (2014). Real-scale investigation of the kinematic response of a rockfall protection embankment. *Natural Hazards and Earth System Sciences*, *14*(6), 1269. https://doi.org/10.5194/nhess-14-1269-2014

Lévy, C., Mangeney, A., Bonilla, F., Hibert, C., Calder, E. S., & Smith, P. J. (2015). Friction weakening in granular flows deduced from seismic records at the Soufriére Hills volcano, Montserrat. *Journal of Geophysical Research: Solid Earth*, *120*, 7536–7557. https://doi.org/10.1002/2015JB012151

Locat, P., Couture, R., Leroueil, S., Locat, J., & Jaboyedoff, M. (2006). Fragmentation energy in rock avalanches. *Canadian Geotechnical Journal*, *43*(8), 830–851. https://doi.org/10.1139/t06-045

Luethi, R., Gruber, S., & Ravanel, L. (2015). Modelling transient ground surface temperatures of past rockfall events: Towards a better understanding of failure mechanisms in changing periglacial environments. *Geografiska Annaler. Series A, Physical Geography*, *97*(4), 753–767. 1–15, https://doi.org/10.1111/geoa.12114

McDowell, G. R., & Bolton, M. (1998). On the micromechanics of crushable aggregates. *Gèotechnique*, *48*(5), 667–679. https://doi.org/10.1680/geot.1998.48.5.667

Morrissey, M. M., Savage, W. Z., & Wieczorek, G. F. (1999). Air blasts generated by rockfall impacts: Analysis of the 1996 Happy Isles event in Yosemite National Park. *Journal of Geophysical Research*, *104*(B10), 23,189–23,198. https://doi.org/10.1029/1999JB900189

Noetzli, J., Gruber, S., Kohl, T., Salzmann, N., & Haeberli, W. (2007). Three-dimensional distribution and evolution of permafrost temperatures in idealized high-mountain topography. *Journal of Geophysical Research*, *112*, F02S13. https://doi.org/10.1029/2006JF000545

Noetzli, J., Huggel, C., Hoelzle, M., & Haeberli, W. (2006). GIS-based modelling of rock-ice avalanches from Alpine permafrost areas. *Computational Geosciences*, *10*(2), 161–178. https://doi.org/10.1007/s10596-005-9017-z

Plafker, G., & Ericksen, G. E. (1978). Nevados Huascaran avalanches, Peru. In B. Voight (Ed.), *Rockslides and avalanches* (Vol. 1, pp. 277–314). Amsterdam: Elsevier.

Planet Team (2017). Planet application program interface. In *Space for Life on Earth*. San Francisco, CA. https://api.planet.com

Ravanel, L., Amitrano, D., Deline, P., Gallach, X., Helmstetter, A., Hobléa, F., & et al. (2016). The small rock avalanche of January 9, 2016 from the calcareous NW pillar of the iconic Mont Granier (1933) m asl, French Alps. In *EGU General Assembly Conference Abstracts* (Vol. 18, p. 13535)

Ravanel, L., & Deline, P. (2008). Le face oust des Drus (massif du Mont-Blanc): evolution del l'instabilité d'une paroi rocheuse dand la haute montagne alpine depuis la fin du petit are glaciaire. *Géomorphologie*, *4*, 261–272.

Rhodes, M. (1998). *Introduction to particle technology* (p. 320). Chichester, UK: Wiley.

Rosin, P. (1933). The laws governing the fineness of powdered coal. *Journal of the Institute of Fuel*, *7*, 29–36.

Rosin, P., & Rammler, E. (1933). Regularities in the distribution of cement particles. *Journal of the Institute of Fuel*, *7*, 29–33.

Simpson, J. E. (1982). Gravity currents in the laboratory, atmosphere, and ocean. *Annual Review of Fluid Mechanics*, *14*(1), 213–234. https://doi.org/10.1146/annurev.fl.14.010182.001241

Sosio, R., Crosta, G. B., & Hungr, O. (2008). Complete dynamic modeling calibration for the Thurwieser rock avalanche (Italian Central Alps). *Engineering Geology*, *100*(1-2), 11–26. https://doi.org/10.1016/j.enggeo.2008.02.012

Sovilla, B., Schaer, M., Kern, M., & Bartelt, P. (2008). Impact pressures and flow regimes in dense snow avalanches observed at the Vallée de la Sionne test site. *Journal of Geophysical Research*, *113*, F01010. https://doi.org/10.1029/2006JF000688

Stock, G. M., Bawden, G. W., Green, J. K., Hanson, E., Downing, G., Collins, B. D., et al. (2011). High-resolution three-dimensional imaging and analysis of rock falls in Yosemite Valley, California. *Geosphere*, *7*(2), 573–581. https://doi.org/10.1130/GES00617.1

Stock, G. M., Collins, B. D., Santaniello, D. J., Zimmer, V. L., Wieczorek, G. F., & Snyder, J. B., (2013). Historical rock falls in Yosemite National Park, California (1857–2011): *U.S. Geological Survey Data Series* 746, 17 p. and data files. http://pubs.usgs.gov/ds/746/

Tromans, D., & Meech, J. A. (2004). Fracture toughness and surface energies of covalent minerals: Theoretical estimates. *Minerals Engineering*, *17*(1), 1–15. https://doi.org/10.1016/j.mineng.2003.09.006

Valero, A., Valero, A., & Cortés, C. (2011). Exergy of comminution and the Crepuscular Planet. In Proceedings of the 6th Dubrovnik Conference on Sustainable Development of Energy Water and Environmental Systems, Dubrovnik, Croatia, September, 25–29

Viero, A., Furlanis, S., Squarzoni, C., Teza, G., Galgaro, A., & Gianolla, P. (2013). Dynamics and mass balance of the 2007 Cima Una rockfall (Eastern Alps, Italy). *Landslides*, *10*(4), 393–408. https://doi.org/10.1007/s10346-012-0338-4

von Rittinger, R. P. (1867). *Textbook of mineral dressing*. Berlin: Ernest and Korn.

Weiss, J., Girard, L., Gimbert, F., Amitrano, D., & Vandembroucq, D. (2014). (Finite) statistical size effects on compressive strength. *Proceedings of the National Academy of Sciences*, *111*(17), 6231–6236. https://doi.org/10.1073/pnas.1403500111

Whalley, W. B. (1974). *The mechanics of high-magnitude, low-frequency rock failure, and its importance in a mountainous area* (pp. 1–48). *Department of Geography*. Reading: University of Reading.

Wieczorek, G. F. (2002). Catastrophic rockfalls and rockslides in the Sierra Nevada, USA. In S. G. Evans & J. V. DeGraff (Eds.), *Catastrophic landslides: effects, occurrence, and mechanisms* (pp. 165–190). America: The Geological Society.

Wieczorek, G. F., Snyder, J. B., Borchers, J. W., & Reichenbach, P. (2007). staircase falls rockfall on December 26, 2003, and geologic hazards at Curry Village, Yosemite National Park, California. U.S. Geological Survey Open-File Report 2007–1378. Retrieved from http://pubs.usgs.gov/of/2007/1378/

Wieczorek, G. F., Snyder, J. B., Waitt, R. B., Morissey, M. M., Uhrhammer, R. A., Harp, E. L., et al. (2000). Unusual July 10, 1996, rock fall at Happy Isles, Yosemite National Park, California. *GSA Bulletin*, *112*(1), 75–85. https://doi.org/10.1130/0016-7606(2000)112<75:UJRFAH>2.0.CO;2

Wieczorek, G. F., Stock, G. M., Reichenbach, P., Snyder, J. B., Borchers, J. W., & Godt, J. W. (2008). Investigation and hazard assessment of the 2003 and 2007 Staircase Falls rock falls, Yosemite National Park, California, USA. *Natural Hazards and Earth System Sciences*, *8*(3), 421–432. https://doi.org/10.5194/nhess-8-421-2008

Zhao, T., Crosta, G. B., Utili, S., & De Blasio, F. V. (2017). Investigation of rock fragmentation during rockfalls and rock avalanches via 3D DEM analyses. *Journal of Geophysical Research: Earth Surface*, *122*, 678–695. https://doi.org/10.1002/2016JF004060

Zimmer, V. L., Collins, B. D., Stock, G. M., & Sitar, N. (2012). Rock fall dynamics and deposition: An integrated analysis of the 2009 Ahwiyah Point rock fall, Yosemite National Park, USA. *Earth Surface Processes and Landforms*, *37*(6), 680–691. https://doi.org/10.1002/esp.3206